Alma Mater Studiorum – Università di Bologna

RESEARCH DOCTORATE
IN ELECTRONICS, COMPUTER SCIENCE
AND TELECOMMUNICATIONS

Scientific Sector Code: ING-INF/02

OPTICAL MICRORING RESONATORS BASED ON ION-IMPLANTED LiNbO$_3$ RIDGE WAVEGUIDES

Doctoral Dissertation of:
Giovanni Battista Montanari

Advisor:
Prof. Paola Mello
Tutor:
Prof. Paolo Bassi
Supervisor:
Prof. Gian Giuseppe Bentini

Cycle XXII

Final exam year 2010

Dedicated to Roberta

Keywords:

Microring Resonators

$LiNbO_3$

Ion-implantation

Ridge waveguides

Contents

List of Figures

List of Tables

Introduction

The growing interest for Integrated Optics for sensing, telecommunications and even electronics is driving research to find solutions to the new challenges issued by a more and more fast, connected and smart world.

This thesis deals with the design, the fabrication and the characterisation of the first prototypes of Microring Resonators realised using ion implanted Lithium Niobate ($LiNbO_3$) ridge waveguides.

Optical Resonator is one among the most important devices for all tasks described above. $LiNbO_3$ is the substrate commonly used to fabricate optical modulators thanks to its electro-optic characteristics. Since it is produced in high quantity, good quality and large wafers its price is low compared to other electro-optic substrate [1].

The possible technologies commonly used to fabricate waveguides in Lithium Niobate are proton exchange and metal diffusion inside the crystal through thermal process [2]. Both these two techniques increase the refractive index changing the crystal density and are limited by the physical diffusivity of LN.

Ion-implantation, instead, is based on the refractive index change caused by the bombardment of charged particles that produces damage into the crystal. So the tailoring of the refractive index profile is possible by the suitable choice of implantation parameters. This allows a much better control on the device footprints.

Moreover, we will show that ion implantation can be employed to enhance the etching rate allowing for surface micro-machining of the material. This process can produce a waveguide with very low roughness observed at the Scanning Electron Microscope (SEM).

Finally it has been assessed a complete technological process for the fabrication of Microring Resonator devices in Lithium Niobate by ion implantation and the first prototypes have been produced.

To achieve these results both the theoretical and the practical point of view were followed simultaneously. Therefore this thesis is structured as follows:

Chapter 1 introduces the resonator theory starting from a simple application: the *Etalon*. Then a view of the possible implementation and application of resonators is given with a particular attention for microring resonators.

Chapter 2 explains the analytical and numerical methods chosen to design the devices and the approximations lying upon they are based.

Chapter 3 analyses Lithium Niobate and its optical and chemical properties modification due to ion-implantation.

Chapter 4 gives a view of the Technological process developed to fabricate our prototypes.

Chapter 5 collects all the results achieved during this work. Starting from the design of the devices, its characterisation, correction and redesign proposal.

Chapter 1

Resonator Theory

In this chapter, the general features of a resonator will be introduced through an example: the *Fabry-Perot Cavity*. The parameters describing the resonator's behavior will be defined and generalised to other device typologies.

1.1 Fabry-Perot Cavity

A Fabry-Perot cavity or *Etalon* is a device constituted by two semi-reflecting mirrors separated by an homogeneous medium thick l. Depending on the application desired, the characteristics of this medium can be different: linear, not linear, lossless or lossy. To describe the working principle let's suppose that the medium interposed between the two mirrors is linear, reciprocal and lossless [3].

Let's consider an incident Plane Wave with arbitrary direction compared to the left mirror normal. It will be reflected and transmitted more and more times by the two discontinuity surfaces (i.e. the mirrors). Considering a ray orthogonal to the wavefronts, a working scheme of the device is illustrated in Figure 1.1.

Now we want to determinate the transfer matrix which describes the behaviour of all the structure [4]. Let (a_1, b_1) and (a_2, b_2) be the direct and reflected wave intensities at the two device surfaces, ϑ_i and ϑ are the angles of the incident and reflected ray respectively, r_1, t_1 and r_2, t_2 are the reflecting and transmitting coefficients of the two mirrors respectively, while R and T are the reflecting and transmitting coefficients of the complete structure. Let's consider $R^2 + T^2$ not strictly unitary to maintain the generality of the problem: while the semi-reflecting surfaces will be always lossless, the interposed medium, with refractive index n, could be lossy or even with an intrinsic gain.

Finally let δ be the phase difference between two successive wavefront introduced by the travelling into the structure. To calculate it, one has to take into account the propagation effect and the reflections and transmissions on each wave-

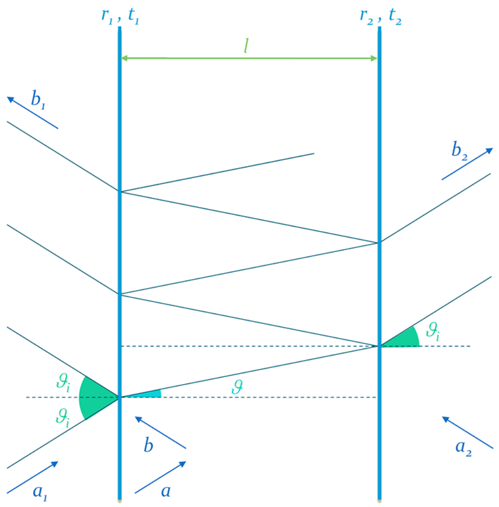

Figure 1.1: *Working scheme of an Etalon*

front. Assuming the air as external medium and recalling the Snell's law, after some calculations one gets [5]:

$$\delta = 2nlk \cos \vartheta \tag{1.1}$$

where k is the vacuum wavenumber.

It's now possible to calculate the shares that, summed all together, make the total transmitted field. Each complete path into the cavity corresponds to a multiplication by $r_1 r_2 e^{-j\delta}$ [5]. So if a is the incoming Plane Wave inside the cavity (see Figure 1.1), its expression is given by:

$$a = \sum_{n=0}^{\infty} \left(r_1 r_2 e^{-j\delta} \right)^n jt_1 a_1 = \frac{jt_1}{1 - r_1 r_2 e^{-j\delta}} a_1 \tag{1.2}$$

Using the equation [5]:

$$\begin{bmatrix} b_1 \\ a \end{bmatrix} = \begin{bmatrix} -r_1 & jt_1 \\ jt_1 & -r_1 \end{bmatrix} \begin{bmatrix} a_1 \\ b \end{bmatrix}$$

after some algebras one arrives at

$$b_1 = \frac{-r_1 + r_2 e^{-j\delta}}{1 - r_1 r_2 e^{-j\delta}} a_1 \quad \text{and} \quad b = -\frac{jt_1 r_2 e^{-j\delta}}{1 - r_1 r_2 e^{-j\delta}} a_1.$$

The outgoing wave from the structure b_2 is a given by (1.2), delayed by a propagation factor of $e^{-j\delta/2}$ and transmitted through the right mirror:

$$b = -\frac{t_1 t_2 e^{-j\delta/2}}{1 - r_1 r_2 e^{-j\delta}} a_1.$$

Since the structure is reciprocal, after repeating all the procedure illustrated above, one arrives at the same results for b_1 and b_2, so we can assume $a_2 = a_1$.

Now the transfer matrix of the etalon ca be written as:

$$S = \frac{1}{1 - r_1 r_2 e^{-j\delta}} \begin{bmatrix} -\left(r_1 - r_2 e^{-j\delta}\right) & -t_1 t_2 e^{-j\delta/2} \\ -t_1 t_2 e^{-j\delta/2} & -\left(r_2 - r_1 e^{-j\delta}\right) \end{bmatrix}. \tag{1.3}$$

1.1.1 Etalon Spectral Characteristics

The law describing the power transmission (transmittance) through the Fabry-Perot cavity is [5]:

$$|H(j\omega)|^2 = \frac{t_1^2 t_2^2}{(1 - r_1 r_2)^2 + 4 r_1 r_2 \sin^2 \delta/2}. \tag{1.4}$$

Till now no hypothesis about the kind of interposed medium or the mirror type were made. Now we will consider a particular case: two equal lossless mirrors ($t_1 = t_2 = t$, $r_1 = r_2 = r$, $t^2 + r^2 = 1$). In this case Eq. (1.4) becomes:

$$|H(j\omega)|^2 = \frac{\left(1 - r^2\right)^2}{(1 - r^2)^2 + 4r^2 \sin^2 \delta/2} = \frac{1}{1 + F \sin^2 \delta/2} \tag{1.5}$$

where

$$F = \frac{4r^2}{(1 - r^2)^2}.$$

So the transmittance depends on frequency. Its maxima are equals to 1 and occur when $\sin^2 \delta/2 = 0$, i.e. when δ is an even multiple of π. In this case, the so called *Resonance Condition*, corresponds to frequency values given by:

$$f_m = \frac{mc}{2nl \cos \vartheta} \tag{1.6}$$

where c is the speed of light. The transmittance maxima are spaced between them by:

$$\Delta f = f_{m+1} - f_m = \frac{c}{2nl \cos \vartheta}. \tag{1.7}$$

The distance Δf is called *Free Spectral Range* (FSR) of the device. This distance can be assumed constant while the refractive index n doesn't change.

The transmittance minima occurs, instead, when $\sin^2 \delta/2 = 1$, i.e. when δ is an odd multiple of π. So the minimum transmittance value is

$$\frac{1}{1 + F} = \frac{\left(1 - r^2\right)^2}{(1 + r^2)^2}.$$

The ratio between the maximum and minimum of the transmittance is called *Extinction Ratio*, its value is $(1 + F)$ and grows as r grows.

The *Full Width at Half Maximum* (FWHM) δf of each maximum is defined as the frequency interval between the two points in the transmittance curve with a value equal to half of the maximum. Under certain approximations [5] it can be written as:

$$\delta f = \frac{c}{\pi n l \cos\vartheta}\frac{1}{\sqrt{F}} = \frac{2\Delta f}{\pi\sqrt{F}}. \tag{1.8}$$

One can introduce the device *Finesse* defined as [5]:

$$\mathfrak{F} = \frac{\Delta f}{\delta f} = \pi\frac{r}{1-r^2}. \tag{1.9}$$

The Finesse gives a quantitative evaluation to the frequency selectivity of the device. In fact, the larger is the reflection coefficient, the larger results the Finesse and so the frequency selectivity (see Figure 1.2).

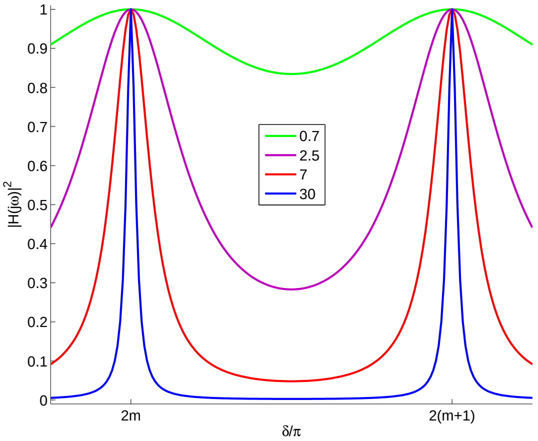

Figure 1.2: *Transmittance spectra of a Fabry-Perot Cavity for different values of the Finesse* $\mathfrak{F}$.

1.1.2 Lossy Etalon

Till now we have considered an ideal cavity without any kind of loss inside it. In a real cavity there are loss due to various reasons. First of all, one has to take into account the attenuation of the propagating field. This loss is due to both the absorption and both the diffusion of interposed medium. It can be described with the term $e^{-\alpha 2l/\cos\vartheta}$ for a complete path inside the cavity. Secondly also the mirrors imperfections have to be considered since they produce a not ideal behaviour in the reflected signal [5]. Another loss mechanism can be the power transfer to radiating modes (i.e. power lost) inside a cavity made with an optical waveguide. Starting from these considerations, Eq. (1.5) has to be rewritten using:

$$r = e^{-\alpha_t l / \cos\vartheta}$$

here α_t is an attenuation coefficient which describes all the loss mechanisms cited above.

With this reflection coefficient Eq. (1.9) becomes:

$$\mathcal{F} = \pi \frac{e^{-\alpha_t l / \cos\vartheta}}{1 - e^{-2\alpha_t l / \cos\vartheta}}. \tag{1.10}$$

The loss presence inside the cavity produce a performance degradation has shown in Figure 1.3.

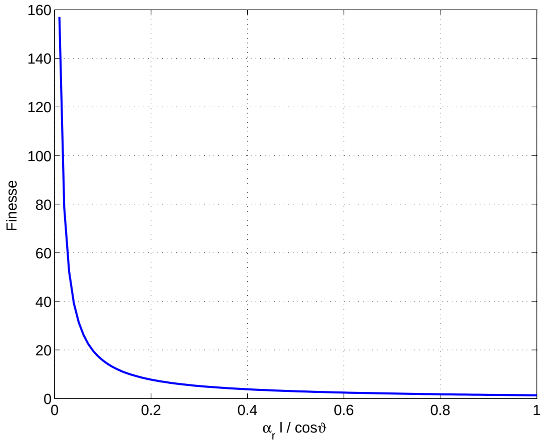

Figure 1.3: *Finesse versus cavity loss factor* $\alpha_t l / \cos\vartheta$

If $\alpha_r l / \cos\vartheta \ll 1$, Eq. (1.10) yields [5]:

$$\mathcal{F} \approx \frac{\pi}{2\alpha_t l / \cos\vartheta}.$$

Considering a paraxial propagation (i.e. $\vartheta = 0$) one obtains, recalling Eq. (1.7) and (1.9):

$$\delta f = \frac{\Delta f}{\mathcal{F}} \approx \frac{c/2nl}{\pi/2\alpha_t l} = \frac{c\,\alpha_t}{n\pi}. \tag{1.11}$$

Since α_r is the effective attenuation coefficient in the space domain, $c\,\alpha_t$ is the effective attenuation coefficient in the time domain. So it's possible to define a cavity time constant of the kind:

$$\tau_t = \frac{1}{c\,\alpha_t}.$$

Then the FWHM can be rewritten as:

$$\delta f = \frac{1}{2\pi\tau_t}.$$

Now it is possible to define the cavity figure of merit Q so-called *Quality factor* as:

$$Q = \frac{2\pi \text{ Energy inside the cavity}}{\text{Energy lost in one period}} = \frac{2\pi}{c\,\alpha_t / f_0} \tag{1.12}$$

where f_0 is the cavity *resonance frequency*. Let's write

$$Q = \frac{f_0}{\delta f} = 2\pi f_0 \tau_t = \frac{2}{n}\frac{f_0}{\Delta f}\mathfrak{F} \tag{1.13}$$

and, since it's reasonable to consider the cavity working frequency much greater than the FSR, it holds also that $Q \gg \mathfrak{F}$.

1.2 Overview of Optical Resonators

Once the main features of a resonator have been derived with reference to a particular example of such a structure, it can also be noticed that many other possible technical solutions realise devices with the same features simply varying the physical mechanism that creates the resonance [6]. Considering this point of view, resonators can be classified depending on:

Confinement by multiple reflection like the Vertical Cavity Surface Emitting Laser (VCSEL) and the Photonic Crystal

Confinement by Total Internal Reflection (TIR) like microresonators based on Spheres, Disks or Rings.

1.2.1 VCSEL

Since the first demonstration in 1979, VCSELs have received much attention primarily because of the interest in the development of high density laser arrays in optical communications and optical interconnect applications. In contrast to a conventional edge emitting diode laser, the light is emitted from the VCSEL perpendicular to the wafer substrate. In simplest terms, a VCSEL consists of a semiconductor laser diode sandwiched vertically between two highly reflective mirrors. The mirrors usually consist of either dielectric or semiconductor distributed Bragg reflectors (DBRs). In this context, a DBR is a multilayer stack of alternating materials where the thickness of each layer is $\lambda/4$. In the centre of the cavity, between the mirrors, there is a either a bulk gain region or one or more *quantum wells*.

VCSELs work taking advantage of the Fabry-Perot Cavity (see section 1.1) made by the two reflective surfaces which confine the field and make it rebound from side to side. The Electromagnetic field is also amplified by stimulated emission inside the active region in the middle of the optical cavity. Examples of this device are given in Figure 1.4 while for an extensive treatment of these devices see [7].

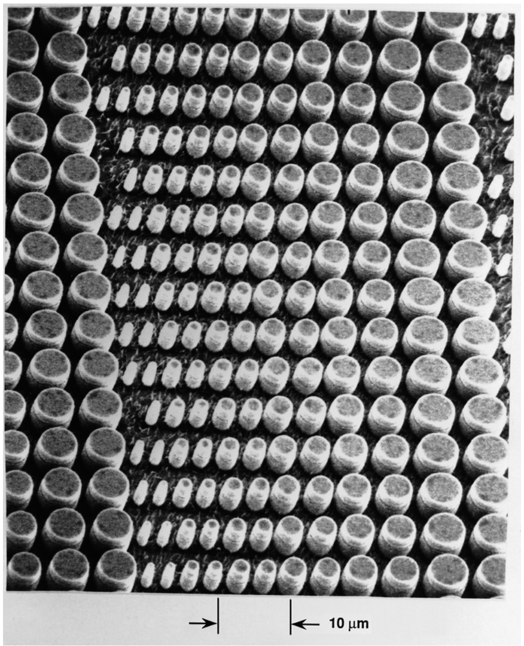

Figure 1.4: *Scanning Electron Microscope (SEM) picture of ion beam etched microlasers with diameters ranging from 1 to* 5 *µm [7].*

1.2.2 Photonic crystals

Photonic crystals are artificial structures that have a periodic variation of the refractive index along one, two, or three dimensions. Analogous to the *energy gap* in pure semiconductor crystals in which electrons are forbidden these photonic bandgap (PBG) structures have a frequency stopband over which there is no transmission of electromagnetic waves. Similar to a donor or acceptor state in a doped semiconductor, a small defect introduced into the photonic crystal creates a resonant mode at a frequency that lies inside the bandgap. The defect in the periodic array behaves as a microcavity resonator. For an example of this kind of devices see Figure 1.5 while for further details see [8].

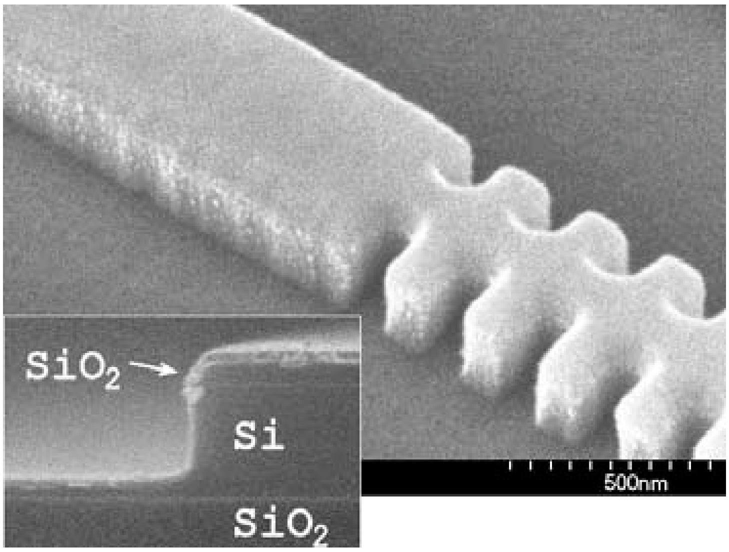

Figure 1.5: *SEM picture of a Photonic Wire Bragg grating fabricated in SOI technology [9].*

1.2.3 Microsphere Resonator

A Microsphere Resonator is a sphere usually in fused silica obtained by melting the core of an optical fibre which drop a perfect sphere. The injection and detection bus-bar are usually made by two optical fibres put at a certain distance from the sphere [10]. This kind of resonator has the best Quality factor (see §1.1.2 and [11]) compared to the Microdisks or Microrings (see paragraph 1.3) and is normally used as a biomedical sensor [12]. For an example of this kind of device see Figure 1.6 while for further details see [13] and [14].

1.2.4 Microring and Microdisk resonators

Microring and Microdisk resonators are based on ring or a disk integrated on a dielectric substrate were the light is injected and detected by two coupled waveguides placed near the resonator [16][17][18]. An example of each device is given in Figure 1.7. In the next section this kind of devices will be illustrated with more detail as they are the core of this work.

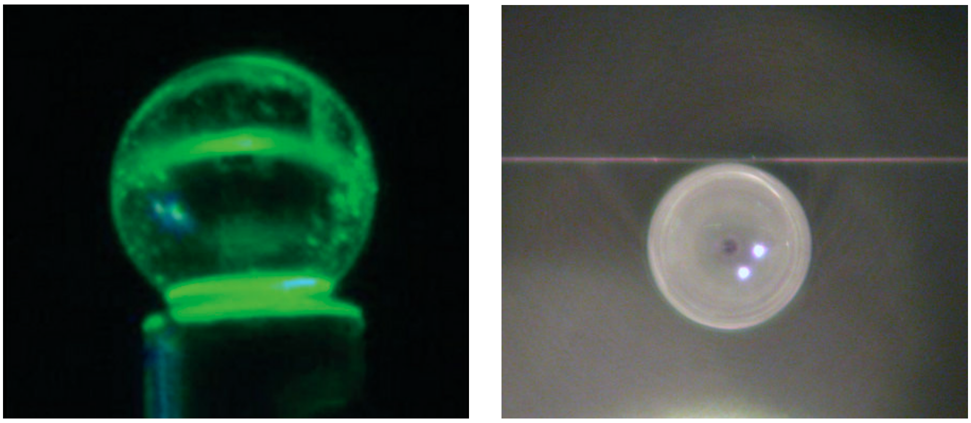

Figure 1.6: *Left: A silicate glass microsphere laser with a diameter of 50 µm during a Green Up-Conversion. Right: top view with laterally coupled optical fibre [15].*

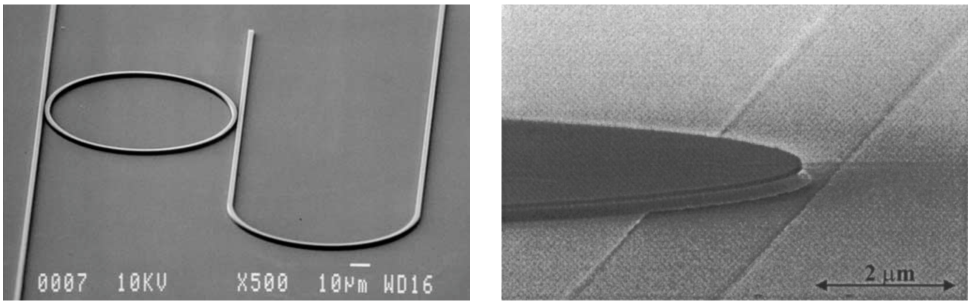

(a) (b)

Figure 1.7: *SEM pictures of (a) a nano-imprinted Polystyrene Microring Resonator between two bus waveguides [19] and (b) a SOI technology based Microdisk Resonator on the top Silicon layer with bus waveguides underneath [20].*

1.3 Circular Optical Microresonators

For this kind of resonators a ring or a disk shaped dielectric cavity is placed between two parallel dielectric straight waveguides. The straight waveguides can be positioned either in the same plane (horizontal coupling scheme, see Figure 1.7a) or below (vertical coupling scheme, see Figure 1.7b) the cavity plane. These two straight waveguides form four ports for the external connections, the two input ports named “In-port” and “Add-port”, and the two output ports named “Through-port” and “Drop-port” (see Figure 1.8).

To understand the functioning of the microresonators, for the sake of simplic-

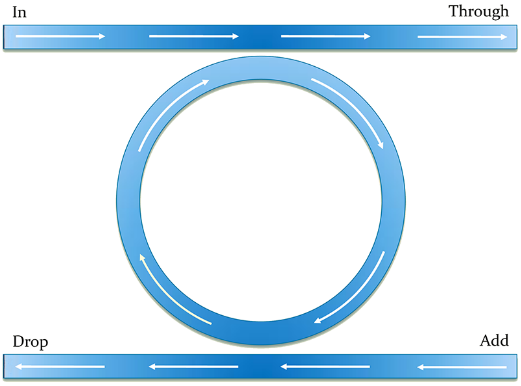

Figure 1.8: *Ports displacement of a circular microresonator.*

ity, only unidirectional fields (clockwise propagating) will be considered, where only the In-port is illuminated, while there is no incoming signal at the Add-port.

Conventionally, the functioning of microresonators is described by the interaction of harmonic optical waves propagating along the straight waveguide and the cavity, and the interferometric resonances of the waves inside the cavity [21].

A single frequency optical wave is launched at the In-port of the resonator. As this signal propagates along the upper straight waveguide, that connects the In-port and Through-port, part of it is evanescently coupled to the cavity. While propagating along the cavity, part of this signal is coupled to the lower straight waveguide and appears at the Drop-port. The remaining part of the signal propagates along the cavity, and interferes with the newly in-coupled signal in the upper interaction region. Depending upon the specific configuration, these two fields undergo constructive or destructive interference.

If the cavity field is out of phase with the newly entering field, then destructive interference takes place inside the cavity and as a result, there is only a small amount of power inside the cavity. This is so-called off resonance conditions. As shown in Figure 1.9a, most of the input power is directly transmitted to the Through-port, and there is small power at the Drop-port.

On the other hand, if the field inside the cavity is in phase with the newly in-coupled signal, then constructive interference occurs an energy increases inside the cavity. This field gets coupled to the Drop-port waveguide. This is so-called resonance conditions and there is a significant power observed at the Drop-port, while much lower power appears at the Through-port. This situation is shown in Figure 1.9b.

A typical spectral response of a microresonator device is shown in Figure 1.10. Resonances appear as dips in the Through-port power curve and peaks in the Drop-port power curve. In other words, the wavelengths for which a microres-

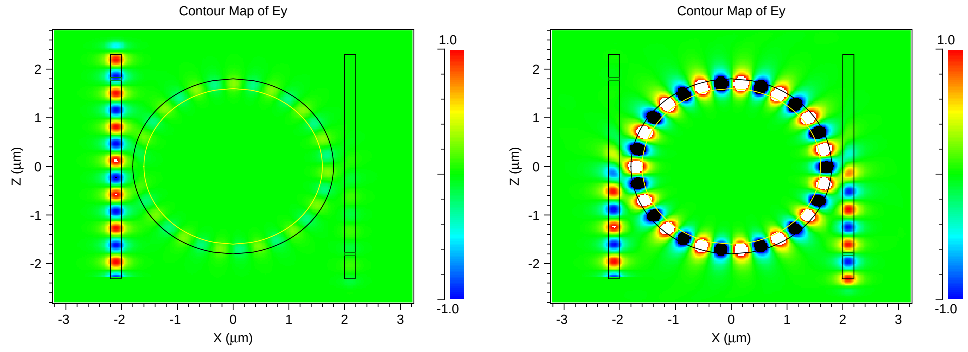

(a)

(b)

Figure 1.9: *Off-resonance state (a) and resonance state (b) of a Microring Resonator.*

onator is on resonance, will be "dropped" at the Drop-port. Also, for a symmetrical device, if a new signal that corresponds to a resonance wavelength is launched at the Add-port, it will get "added" to the off resonance signal launched at the In-port, and appears at the Through-port. Therefore the arrangement shown can be used as an add/drop filter.

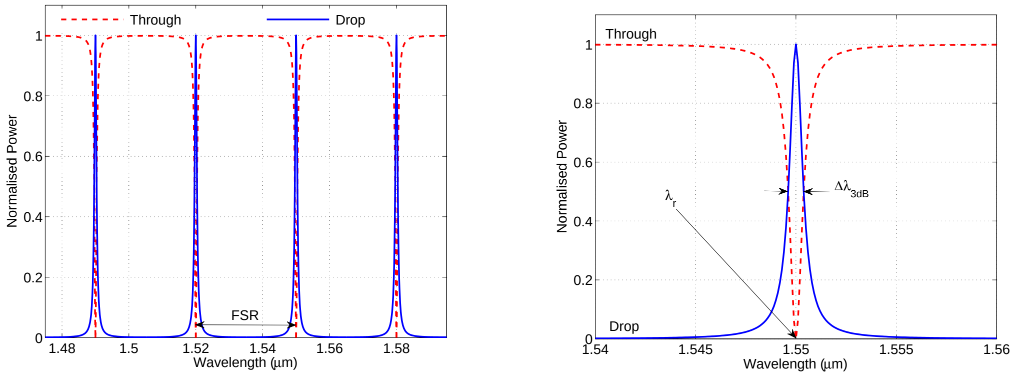

Figure 1.10: *Spectral response of a microring resonator.*

1.4 Existing approaches for modelling of circular microresonators

From §1.1.2 we know that the spectral response of a Fabry-Perot cavity depends on the propagation of electromagnetic fields along the cavity and the quality of the mirrors. Following the same procedure [22][23] is possible, in first approximation, to describe the spectrum of a microring or microdisk resonator as a function of the geometrical parameters like the size of the cavity, the gap widths between the cavity and the straight waveguides, and by material parameters like refractive indices.

Several analytical, parametrical, pure numerical, and mixed analytical & numerical models have been proposed for the analysis of these structures. Proper understanding of the propagation of electromagnetic fields in the cavity is very important, because the behavior of these fields is mainly responsible for the resonances in the spectral response. This is explained by a time domain model of isolated (circular) cavities in terms of integer valued angular mode number and complex valued eigenfrequencies [24]. But in the case of the ring resonators analysed, fabricated and characterized in this work, the cavity is coupled to two external straight waveguides. Since these bus waveguides are usually modelled in terms of given real valued frequency a complex eigenfrequency model of (isolated) cavities is not the most suitable choice to study a cavity coupled to straight waveguides, in fact one have to match the two frequencies to get the complete device behaviour.

For this reason, in literature, the coupling between a circular cavity and a straight waveguide has been modelled with phenomenologically derived expressions for the coupling coefficient [16], and with different versions of the *Coupled Mode Theory* [25]. Coupled mode theory [5] proved to be a quite useful tool for the analysis of the interaction between straight waveguides.

Concerning the modeling of three dimensional microresonators, by using the *Effective Index Method* (EIM, see §2.1.1) certain 3-D structures can be reduced to 2-D ones. These are then analyzed by means of phenomenologically derived expressions for the coupling coefficients [26] or by conformal mapping method [27].

Apart from the above analytical and parametrical methods, pure numerical methods like Finite Difference Time Domain (FDTD) [6] are also used for the simulation of microresonators. Since they are heavily time consuming, in case of the 3-D structure the use of this approach becomes prohibitive. These simulation approaches are generally reserved for benchmarking of the results obtained with other techniques and not for practical design.

In the next chapter it will then be shown which methods, among the ones cited above, can be used to calculate the geometrical parameters taking into account the technological specifications of our approach. Their theoretical basis will be introduced, their features described and application issues mentioned and commented. In Chapter 5 these methods will be used to design and interpret measurement results.

Chapter 2

Modelling

In this chapter we will introduce all the methods used in this work to design a microresonator. As shown in §1.4 one can decide to use a complete analytical approach an then try to correct it after the first fabrication process deriving some effective design parameters both physical and geometrical.

This approach is suitable for a well known technology like *SOI* (Silicon On Insulator, see [28]) but in our case, where the technology used is still in a developing phase, as it will be shown in Chapters 3 and 4, one needs also to use numerical simulations to validate the approximations used in the analytic approach.

So in the next sections we will show the two approaches: analytic and numerical simulation based. The case of study will be a microring resonator called racetrack because the two coupling regions between the ring and the bus-bars are made by two straight coupled waveguides. This layout was chosen for technological reasons that will be explained in §4.1. A device scheme and an example in SOI technology are given in Figure 2.1.

2.1 Analytic Approach

The methods explained in this section are used for a 2-D structure. Before using them we need to transform a real 3-D structure to a 2-D one. This is possible, under certain approximations, applying the Effective Index Method that will be illustrated in the next section.

2.1.1 Effective Index Method

Through the EIM the section of a confined structure becomes a planar waveguide with the same propagation characteristics. Usually this reduction of one dimension is widely used, to save both memory occupation and computational

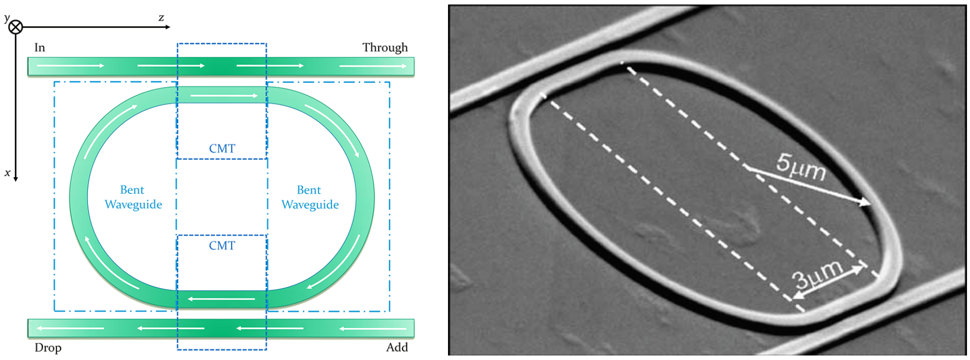

(a) (b)

Figure 2.1: *Racetrack microring resonator. (a) Device scheme indicating the two analytical model used: Bent waveguide model (see §2.1.2) and Coupled Mode Theory (see §2.1.3). (b) Racetrack resonator in SOI. The waveguide width is* 500 *nm, the gap width is* 230 *nm [29].*

time, in the propagation study of cylindrical structures [4]. In this case, one of the two remaining dimensions is the propagation coordinate z and the other is the transverse one, x in our case (see Figure 2.1).

The method resolves the Scalar Helmholtz Equation [5] for cylindrical structures:

$$\frac{\partial^2 U}{\partial x^2} + \frac{\partial^2 U}{\partial y^2} + \left(k^2 n^2(x,y) - \gamma^2\right) U = 0 \tag{2.1}$$

where $U = E_x, E_y$ depending on which polarisation, TE or TM respectively, is under investigation, k is the vacuum wavenumber, $n(x,y)$ the refractive index distribution on the input plane (i.e. xy plane) and γ is the complex valued propagation constant.

If a direction exists along which the refractive index is slowly variable, for example y, one can assume:

$$U(x,y) = \Phi_y(y)\Phi_{xy}(x,y) \tag{2.2}$$

with $\Phi_{xy}(x,y)$ slowly variable with y. Substituting Eq. (2.2) into (2.1) yields:

$$\begin{aligned}\Phi_y(y)\frac{\partial^2 \Phi_{xy}(x,y)}{\partial x^2} + \frac{\partial}{\partial y}\left[\frac{d\Phi_y(y)}{dy}\Phi_{xy}(x,y) + \Phi_y(y)\frac{\partial \Phi_{xy}(x,y)}{\partial y}\right] = \\ = -\left(k^2 n^2(x,y) - \gamma^2\right)\Phi_y(y)\Phi_{xy}(x,y).\end{aligned}$$

After some calculations one gets:

$$\begin{aligned}\Phi_{xy}(x,y)\frac{d^2\Phi_y(y)}{dy^2} + 2\frac{d\Phi_y(y)}{dy}\frac{\partial\Phi_{xy}(x,y)}{\partial y} + \\ + \Phi_y(y)\left[\frac{\partial^2\Phi_{xy}(x,y)}{\partial x^2} + \frac{\partial^2\Phi_{xy}(x,y)}{\partial y^2}\right] = \\ = -\left(k^2n^2(x,y) - \gamma^2\right)\Phi_y(y)\Phi_{xy}(x,y).\end{aligned}$$

Since we assumed that $\Phi_{xy}(x,y)$ changes very slow with y, the:

$$\frac{\partial\Phi_{xy}(x,y)}{\partial y} \approx 0 \quad \text{and} \quad \frac{\partial^2\Phi_{xy}(x,y)}{\partial y^2} \approx 0$$

are well satisfied.

Then the equation to be solved becomes:

$$\begin{aligned}\Phi_{xy}(x,y)\frac{d^2\Phi_y(y)}{dy^2} + \Phi_y(y)\frac{\partial^2\Phi_{xy}(x,y)}{\partial x^2} = \\ = -\left(k^2n^2(x,y) - \gamma^2\right)\Phi_y(y)\Phi_{xy}(x,y).\end{aligned}$$

Dividing by $\Phi_y(y)\Phi_{xy}(x,y)$ one obtains:

$$\begin{aligned}\frac{1}{\Phi_y(y)}\frac{d^2\Phi_y(y)}{dy^2} + \frac{1}{\Phi_{xy}(x,y)}\frac{\partial^2\Phi_{xy}(x,y)}{\partial x^2} + \\ + \left(k^2n^2(x,y) - \gamma^2 + k^2n_{eff}^2(y) - k^2n_{eff}^2(y)\right) = 0\end{aligned}$$

after adding and subtracting $k^2n_{eff}^2(y)$ from the last term. Finally one obtains the two equations:

$$\frac{d^2\Phi_{xy}(x,y)}{dx^2} + \left(k^2n^2(x,y) - k^2n_{eff}^2(y)\right) = 0 \tag{2.3}$$

$$\frac{d^2\Phi_y(y)}{dy^2} + \left(k^2n_{eff}^2(y) - \gamma\right) = 0 \tag{2.4}$$

where (2.4) depends only on y. In Eq. (2.3) ∂x was substituted by dx since $\Phi_{xy}(x,y)$ is slowly variable with y and so one can assume that it varies only with x.

So the EIM asks to solve (2.3) to determinate both $n_{eff}(y)$ and $\Phi_{xy}(x,y)$. Then $n_{eff}(y)$ can be substituted into Eq. (2.4) that, after been resolved, yields both γ and $\Phi_y(y)$. This procedure has to be repeated for each waveguide mode.

Now it's possible to introduce the Bent waveguide model used to compute the bending loss of a microring resonator.

2.1.2 Bent Waveguides

Let's consider a bent slab waveguide with the y-axis as the axis of symmetry as shown in Figure 2.2. We assume that the material properties and the fields do not vary in the y-direction. Being specified by the radially dependent refractive index $n(r)$ (here n is piecewise constant), the waveguide can be seen as a structure that is homogeneous along the angular coordinate θ. Hence one chooses an ansatz for the bend modes with pure exponential dependence on the azimuthal angle, where the angular mode number is commonly written as a product γR with a reasonably defined bend radius R, such that γ can be interpreted as a propagation constant.

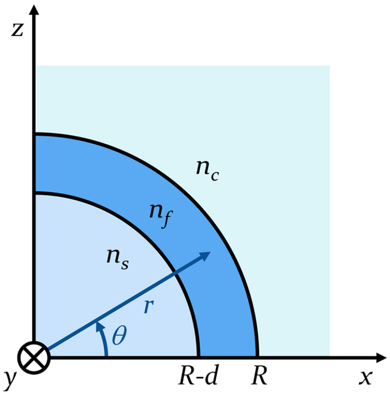

Figure 2.2: *A bent slab waveguide. The core of thickness d and refractive index n_f is embedded between an interior medium ("substrate") with refractive index n_s and an exterior medium ("cladding") with refractive index n_c. The distance between the origin and the outer rim of the bend defines the bend radius R.*

Eigenvalue problem formulation

In the cylindrical coordinate system (r, y, θ), the functional form (in the usual complex notation) of the propagating electric field $\overline{\mathbf{E}}$ and the magnetic field $\overline{\mathbf{H}}$ reads

$$\begin{aligned}\overline{\mathbf{E}}(r,\theta,t) &= (\overline{E}_r, \overline{E}_y, \overline{E}_\theta)(r)e^{j(\omega t-\gamma R\theta)}\\ \overline{\mathbf{H}}(r,\theta,t) &= (\overline{H}_r, \overline{H}_y, \overline{H}_\theta)(r)e^{j(\omega t-\gamma R\theta)}\end{aligned} \tag{2.5}$$

where γ is the propagation constant of the bend mode, and ω is the angular frequency corresponding to vacuum wavelength λ.

Since an electromagnetic field propagating through a bent waveguide looses energy due to radiation [30],γ is complex valued, denoted as $\gamma = \beta - j\alpha$, where β and α are the real valued phase propagation and attenuation constants. Note that the angular behaviour of the field (2.5) is determined by the product γR, where the definition of R is arbitrary.

Given a bend mode, the values assigned to the propagation constant change, if the same physical solution is described by using different definitions of the bend radius R. The definition of the bend radius R as the radial position of the outer interface of the core layer is still applicable when the guiding is effected by a single dielectric interface only, i.e. for the description of whispering gallery modes [31].

If the ansatz (2.5) is inserted into the Maxwell equations, one gets the two separate sets of equations

$$\left.\begin{aligned} \frac{\gamma R}{r} E_y &= -\mu_0 \omega H_r \\ \frac{\partial E_y}{\partial r} &= -j\mu_0 \omega H_\theta \\ \frac{1}{r}\frac{\partial r H_\theta}{\partial r} + \frac{j\gamma R}{r} H_r &= -j\varepsilon_0 \varepsilon \omega E_y \end{aligned}\right\} \text{TE} \tag{2.6}$$

and

$$\left.\begin{aligned} \frac{\gamma R}{r} H_y &= \varepsilon_0 \varepsilon \omega E_r \\ \frac{\partial H_y}{\partial r} &= j\varepsilon_0 \varepsilon \omega E_\theta \\ \frac{1}{r}\frac{\partial r E_\theta}{\partial r} + \frac{j\gamma R}{r} E_r &= j\mu_0 \omega H_y \end{aligned}\right\} \text{TM} \tag{2.7}$$

with vacuum permittivity ε_0, vacuum permeability μ_0, and relative permittivity $\varepsilon = n^2$.

For transverse electric (TE) waves the only nonzero components are E_y, H_r and H_θ, which are expressed in terms of E_y, while for transverse magnetic (TM) waves the only nonzero components are H_y, E_r and E_θ, which are given by H_y. Within radial intervals with constant refractive index n, the basic electric and magnetic components are governed by a Bessel equation with complex order γR:

$$\frac{\partial^2 \phi}{\partial r^2} + \frac{1}{r}\frac{\partial \phi}{\partial r} + (n^2 k^2 - \frac{\gamma^2 R^2}{r^2})\phi = 0 \tag{2.8}$$

for $\phi = E_y$ or $\phi = H_y$, where $k = 2\pi/\lambda$ is the (given, real) vacuum wavenumber. For TE modes, the interface conditions require continuity of E_y and of $\partial_r E_y$ across the dielectric interfaces. For TM modes, continuity of H_y and of $\partial_r H_y$ across the interfaces is required.

Eq. (2.8), together with the interface conditions and suitable boundary conditions for $r \to 0$ and $r \to \infty$, represents an eigenvalue problem with the bend mode profiles ϕ as eigenfunctions, and the propagation constants γ or angular mode numbers $\nu = \gamma R$ as eigenvalues.

The equation is solved piecewise in the regions with constant refractive index. While the procedure is in principle applicable for arbitrary multilayer bent waveguides, for the sake of brevity we discuss here the three layer configuration as introduced in figure 2.2.

The general solution of Eq. (2.8) is a linear combination of the *Bessel functions* of the first kind J and of the second kind Y. This representation is applicable to the core region. Since Y tends to $-\infty$ if $r \to 0$, for the boundedness of the electric/magnetic field at the origin one selects only the Bessel function of the first kind J for the interior region. In the outer region, we are looking for a complex superposition of J and Y that represents outgoing waves. Such a solution can be given in terms of the Hankel functions of the first kind $H^{(1)}$ or of the second kind $H^{(2)}$. Using the asymptotic expansions of these functions [32]:

$$\begin{aligned} H^{(1)}_\nu(nkR) &\sim \sqrt{\frac{2}{\pi nkr}} e^{j(nkr-\nu\pi/2-\pi/4)} \\ H^{(2)}_\nu(nkR) &\sim \sqrt{\frac{2}{\pi nkr}} e^{-j(nkr-\nu\pi/2-\pi/4)} \end{aligned} \tag{2.9}$$

and taking into account the harmonic time dependence $e^{j\omega t}$ (with positive frequency), one observes that $H^{(1)}$ represents incoming waves, while outgoing waves are given by $H^{(2)}$. Thus the piecewise ansatz for the basic components of the electric/magnetic bent mode profile is

$$\phi(r) = \begin{cases} A_s J_\nu(n_s kr) & \text{if } 0 \le r < R^- \\ A_f J_\nu(n_f kr) + B_f Y_\nu(n_f kr) & \text{if } R^- \le r < R^+ \\ A_c H^{(2)}_\nu(n_c kr) & \text{if } r \ge R^+ \end{cases} \tag{2.10}$$

where $R^- = R - d$, $R^+ = R$, and where A_s, A_f, B_f and A_c are so far unknown constants.

The polarisation dependent interface conditions lead to a homogeneous system of linear equations for A_s, A_f, B_f and A_c. The condition for a nontrivial solution can be given in the form

$$\frac{\dfrac{J_\nu(n_f kR^-)}{J_\nu(n_s kR^-)} - q_s \dfrac{J'_\nu(n_f kR^-)}{J'_\nu(n_s kR^-)}}{\dfrac{Y_\nu(n_f kR^-)}{J_\nu(n_s kR^-)} - q_s \dfrac{Y'_\nu(n_f kR^-)}{J'_\nu(n_s kR^-)}} = \frac{\dfrac{J_\nu(n_f kR^+)}{H^{(2)}_\nu(n_c kR^+)} - q_c \dfrac{J'_\nu(n_f kR^+)}{H^{(2)\prime}_\nu(n_c kR^+)}}{\dfrac{Y_\nu(n_f kR^+)}{H^{(2)}_\nu(n_c kR^+)} - q_c \dfrac{Y'_\nu(n_f kR^+)}{H^{(2)\prime}_\nu(n_c kR^+)}} \tag{2.11}$$

with $q_j = n_f/n_j$ for TE polarisation, and with $q_j = n_j/n_f$ for TM polarised fields, for $j = s, c$. Eq. (2.11) is the *dispersion equation for the three layer bent slab waveguide*. For given frequency ω, this equation has to be solved to get the propagation constants $\gamma = \nu/R$.

Bend mode normalisation

The power flow density associated with a bend mode is given by the time averaged Poynting vector $\overline{\mathbf{S}}_{av} = \frac{1}{2}\Re\left[\overline{\mathbf{E}} \times \overline{\mathbf{H}}^*\right]$. The axial component $S_{av,y}$ vanishes in the 2-D setting. For TE waves the radial and azimuthal components are

$$\begin{aligned} S_{av,r} &= -\frac{1}{2\mu_0\omega}\,\Re\left[jE_y\frac{\partial E_y^*}{\partial r}\right]e^{-2\alpha R\theta} \\ S_{av,\theta} &= \frac{\beta}{2\mu_0\omega}\frac{R}{r}|E_y|^2 e^{-2\alpha R\theta} \end{aligned} \tag{2.12}$$

and for TM polarisation one obtains

$$\begin{aligned} S_{av,r} &= \frac{1}{2\varepsilon_0\varepsilon\omega}\,\Re\left[jH_y\frac{\partial H_y^*}{\partial r}\right]e^{-2\alpha R\theta} \\ S_{av,\theta} &= \frac{\beta}{2\varepsilon_0\varepsilon\omega}\frac{R}{r}|H_y|^2 e^{-2\alpha R\theta} \end{aligned} \tag{2.13}$$

The total optical power transported by the mode in the angular direction is given by $P_\theta(\theta) = \int_0^\infty S_{av,\theta}\mathrm{d}r$. Following the procedure explained in [25] one gets the two expressions:

$$\begin{aligned} P_\theta(\theta) &= \frac{|A_c|^2}{2\mu_0\omega\alpha R\pi}e^{\alpha R(\pi-2\theta)} \qquad (TE) \\ P_\theta(\theta) &= \frac{|A_c|^2}{2\varepsilon_0 n_c^2\omega\alpha R\pi}e^{\alpha R(\pi-2\theta)} \quad (TM) \end{aligned} \tag{2.14}$$

for the modal power of TE and TM polarised modes, respectively. For further details about this normalisation and the orthogonality of bend modes see [25].

Simulation Results

To solve the eigenvalue problem (2.11) a bend mode solver was implemented both in MATLAB and FORTRAN 90 following the consideration explained in [25]. This solver yields complex propagation constants and mode profiles in terms of Eq. (2.10).

Table 2.1 lists values for angular mode numbers obtained with the mode solver for the same bend configuration adopted in [25], together with reference data from that source. Since the real parts of $\nu = \gamma R$ resulted equals we put the accent on the image parts with a good overall agreement, for both the developed implementations.

For many applications one is interested at the variation of the phase constant β/k and the attenuation α with the curvature of the bend, expressed by the bend radius R. Figure 2.3 shows corresponding plots for the configuration of Table 2.1.

$R[\mu m]$	$\Re\,[\gamma R]$	$\Im\,[\gamma R]$		
		Reference [25]	MATLAB	FORTRAN
50.5	$4.0189 \cdot 10^{2}$	$-7.9973 \cdot 10^{-2}$	$-7.9974 \cdot 10^{-2}$	$-7.9974 \cdot 10^{-2}$
100.5	$8.0278 \cdot 10^{2}$	$-9.6032 \cdot 10^{-4}$	$-9.6030 \cdot 10^{-4}$	$-9.6054 \cdot 10^{-4}$
150.5	$1.2039 \cdot 10^{3}$	$-7.3914 \cdot 10^{-6}$	$-7.3920 \cdot 10^{-6}$	$-7.4350 \cdot 10^{-6}$
200.5	$1.6051 \cdot 10^{3}$	$-4.8976 \cdot 10^{-8}$	$-5.5151 \cdot 10^{-8}$	$\left(+9.8629 \cdot 10^{-7}\right)$

Table 2.1: *TE_0 angular mode numbers ν for bent waveguides of different bend radius R according to figure 2.2, with $(n_s, n_f, n_c) = (1.6, 1.7, 1.6)$, $d = 1\ \mu m$, for a vacuum wavelength $\lambda = 1.3\ \mu m$.*

As expected, for low curvature the value of β/k tend to the effective index of a straight slab waveguide with equivalent refractive index profile (Figure 2.3a).

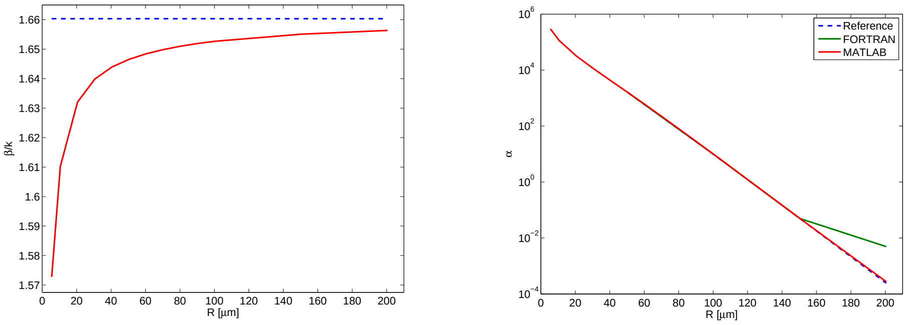

(a) (b)

Figure 2.3: *Simulation results for bends according to Table 2.1. (a) Phase constant β versus the bend radius R. The dashed line indicates the level of the effective index of a straight waveguide with the cross section and refractive index profile of the bent slabs. (b) Attenuation constant α versus the bend radius R* for the two different implementations.

In Figure 2.3b is shown that for low bend radii the agreement with [25] is very good. In fact there is only a strange value in the FORTRAN implementation due by numerical fluctuation (see the last row in Table 2.1).

With the present (semi) analytic solutions at hand, we have now a possibility to validate "classical" expressions for the variation of the bend attenuation with the bend radius. Beyond the high curvature region, Figure 2.3b shows a strict exponential decay of α with respect to R, as predicted by an approximate loss formula given in [33] for symmetric bent slabs:

$$\alpha = \frac{R-w}{R}\,\frac{g^2}{2\beta_s(1+gw)}\,\frac{h^2}{(n_f^2-n_s^2)k^2}\,e^{2gw}e^{-2\left(\beta_s \tanh^{-1}(g/\beta_s)-g\right)(R-w)}. \qquad (2.15)$$

Here β_s is the propagation constant corresponding to the straight waveguide with the width $d = 2w$ and refractive index profile (n_s, n_f, n_s) of the bent waveguide under investigation. Derived quantities are $g^2 = \beta_s^2 - n_s^2 k^2$ and $h^2 = (n_f^2 - n_s^2)k^2 - g^2$. Figure 2.4 reveals a very good agreement with the attenuation constant calculated by our procedure.

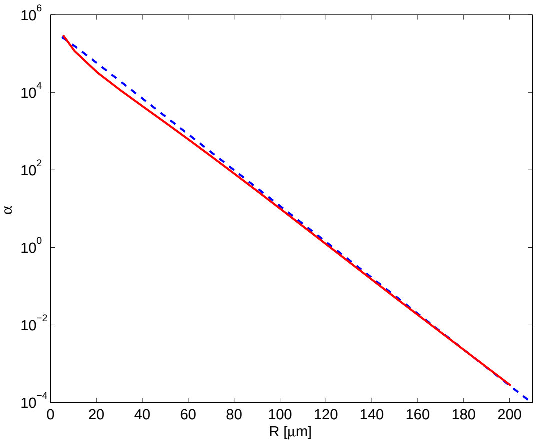

Figure 2.4: *Attenuation constant of the TE_0 mode for symmetric bent waveguides with $n_f = 1.7$, $n_s = n_c = 1.6$, $d = 1$ μm, $\lambda = 1.3$ μm, for varying bend radius R. The dashed line show the exponential decay according to Eq.* (2.15)*, the solid curve is the present analytic mode solver implemented in MATLAB.*

So, Eq. (2.15) can be used when one wants to minimise bending losses since it works better for large bending radii.

Mode profiles

Beyond the values of the propagation constants, the present analytical mode solver permits to evaluate modal fields for the full range of radial coordinates. Figure 2.5 illustrates normalised profiles for the TE_0 bend modes considered in Table 2.1.

One observes the expected effects [33]: bends with large radii R support modes with almost the familiar symmetric, well confined plane profiles of straight symmetric slab waveguides (see [5]). With decreasing bend radius, the phase profiles of the bend modes become more and more curved. Along with the increasing attenuation, the maximum in the absolute value of the basic electric field shifts towards the outer rim of the bend, and the relative field levels in the exterior region grow. The mode profiles are essentially complex, with oscillatory behaviour of the real and imaginary parts of the field profiles in the exterior region.

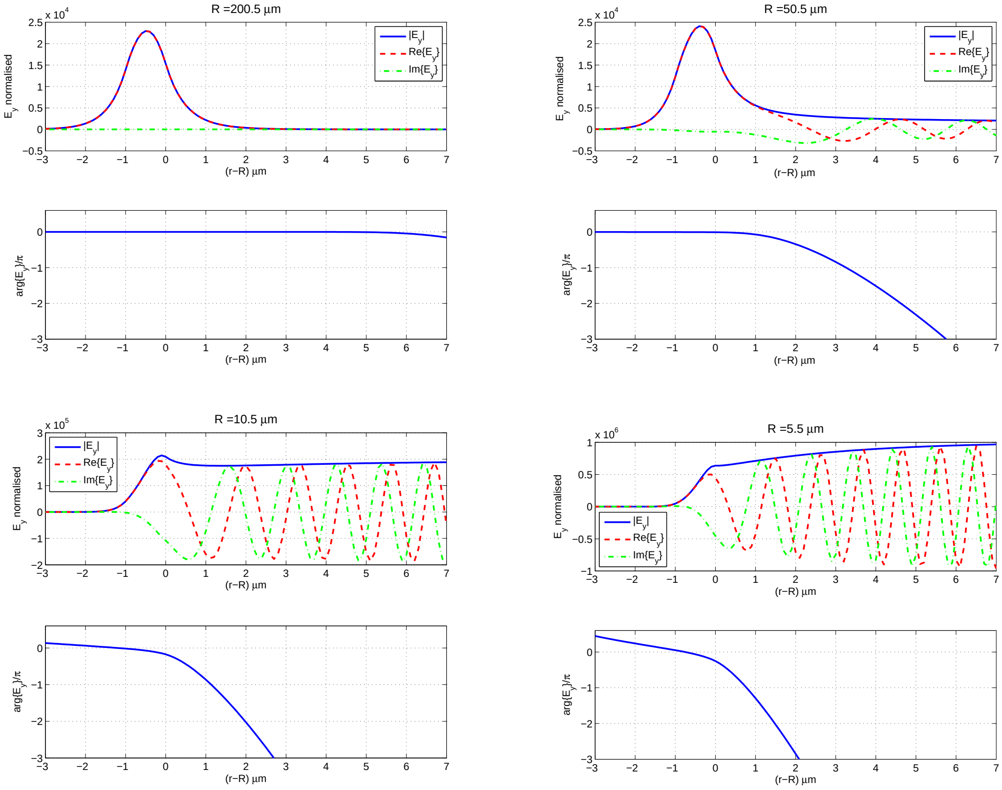

Figure 2.5: *TE_0 mode profiles for bent waveguides according to the setting of Table 2.1, with different bend radii $R = 200.5, 50.5, 10.5, 5.5$ µm. Radial dependence of the absolute value (solid line), the real and imaginary part (dashed and dash-dotted lines) and the phase of the basic electric field component E_y. The profiles are normalised according to Eq. (2.14), with the global phase adjusted such that $E_y(R)$ is real and positive.*

Now that we know how to calculate bending losses and bent mode profiles we can proceed with the modeling of the coupler constituted by two straight waveguides (see Figure 2.1).

2.1.3 Coupled mode theory

In this section we will focalise our attention on a particular application of the CMT: the co-directional coupling between two mono-modal waveguides. The three hypotheses that lie under this method are [5]:

1. The radiation part of the electromagnetic field can be ignored since it is well confined inside the waveguide. So the modes can't be leaky or lossy.

2. There are no sensible variation in the propagation direction. The phase constant β can be then considered unchanged. In other words the structure is cylindrical.

3. The superposition principle is applicable, so the superstructure mode is equivalent to the sum of each separate waveguide mode.

As it will be shown in the next chapters, since the technology used to fabricate our devices is based on ridge waveguides, all these hypotheses are fulfilled.

Coupling coefficient

Let's recall the co-directional coupling coefficient between two mono-modal waveguides [5]:

$$\kappa = \frac{\omega}{4} \int_{S_2} \Delta\varepsilon \, \overline{E}_{t2} \cdot \overline{E}^*_{t1} \, dS \tag{2.16}$$

where the indices 1 and 2 indicate the two waveguides and t stands for transverse.

Now, in the case of two equal waveguides, one can introduce the *coupling length* defined as

$$L_c = \frac{\pi}{2|\kappa|}. \tag{2.17}$$

At this propagation distance, in fact, the power transfer from one waveguide to the other is complete.

Coupler transfer matrix

In Figure 2.6 is reported the scheme of the coupler region pointed out in Figure 2.1. Under the conditions that a single unidirectional mode of the resonator is excited and that the coupling is lossless, one can describe the interaction by the matrix relation [34]:

$$\begin{bmatrix} b_w \\ b_r \end{bmatrix} = \begin{bmatrix} \tau & \eta \\ \eta^* & -\tau^* \end{bmatrix} \begin{bmatrix} a_w \\ a_r \end{bmatrix}$$

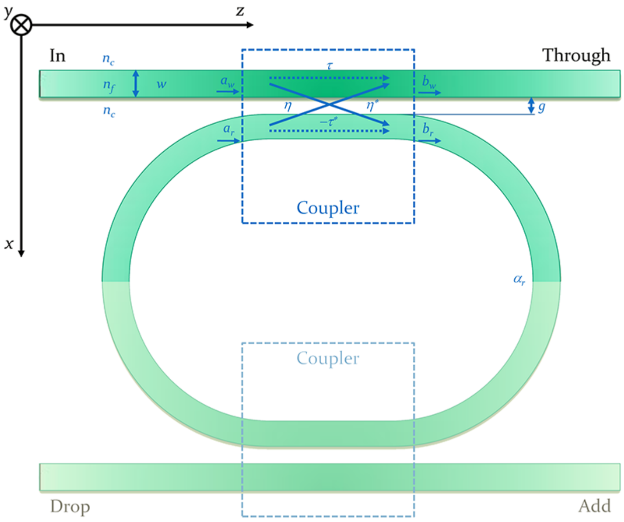

Figure 2.6: *Generic description of dielectric waveguide coupled to ring resonator.*

where the complex mode amplitudes a_w,b_w and a_r,b_r are normalised such that their squared magnitude corresponds to the modal power. The coupling matrix is unitary so that:

$$|\eta|^2 + |\tau|^2 = 1$$

Now, it is useful to write here the more general formulation of Eq. (2.17) [5]:

$$L_{c_\eta} = \frac{\arcsin|\eta|}{|\kappa|}. \tag{2.18}$$

Eq. (2.18) represents the coupling length at which the power transferred to the second guide (i.e. the ring) is equal to $|\eta|^2$ times the input power. Note that, when $\eta = 1$, Eq. (2.18) becomes (2.17).

Ring coupling

Let's recall Figure 2.6. In the following, we will choose that input wave $a_w = 1$ W so that all the field amplitudes will be normalised to a_w. The transmission around the ring is given by

$$a_r = \alpha_r e^{j\delta} b_r$$

where α_r, the inner circulation factor, is real and δ is the phase difference between the two waves inside the ring. The factor α_r represents all the loss mechanisms inside the ring (e.g. by bending loss, material absorption, and sidewalls roughness). Note that for zero internal loss $\alpha_r = 1$.

Following the calculation shown in [34], at resonance one gets:

$$|b_w|^2 = \frac{(\alpha_r - |\tau|)^2}{(1 - \alpha_r|\tau|)^2} \quad \text{and} \quad |a_r|^2 = \frac{\alpha_r^2(1 - |\tau|)^2}{(1 - \alpha_r|\tau|)^2} \tag{2.19}$$

The first part of Eq. (2.19) is of special interest. It shows that when $\alpha_r = |\tau|$, i.e. when the internal losses (represented by α_r) are equal to the coupling losses represented by $|\tau|$, the transmitted power vanishes, i.e. $|b_w|^2 = 0$. This condition, known in the microwave field as that of *critical coupling* [34], is due to perfect destructive interference inside the outgoing waveguide between the transmitted field τa_r and the internal field coupled into the output waveguide ηa_r. An other important thing is that when $\alpha_r|\tau| = 1$, one obtains, according to Eq. (2.19), infinite transmission, i.e. laser oscillation.

Note that all these results depend only on τ and α_r. They are independent of the details of the coupling and those of the resonator. Their simplicity and form are reminiscent of the basic relations describing the Fabry-Perot etalon (see §1.1).

Ring resonator fundamental parameters

In this subsection the same parameters pointed out for the Etalon in §1.1.2 are reported for the microring resonator as wavelength function [25] (see Figure 1.10).

So the FSR can be written has:

$$\Delta\lambda = \frac{\lambda^2}{n_{eff}L_{cav}} \tag{2.20}$$

where λ is the resonance wavelength, L_{cav} is the cavity length and n_{eff} can be replaced by the group effective index [5]:

$$n_{eff,g} = n_{eff} - \lambda\frac{\partial n_{eff,}}{\partial\lambda}$$

when the waveguide and ring dispersions are not negligible.

The FWHM, in the following indicated with $\Delta\lambda_{3dB}$, is

$$\Delta\lambda_{3dB} = \frac{\lambda^2}{\pi n_{eff}L_{cav}}\frac{1 - \alpha_r^2|\tau|^2}{\alpha_r|\tau|} \tag{2.21}$$

that in the best case possible, i.e. when $\alpha_r = |\tau| \approx 1$, reduces to:

$$\Delta\lambda_{3dB} = \frac{\lambda^2(1 - |\tau|^2)}{\pi n_{eff}L_{cav}} = \frac{\lambda^2|\eta|^2}{\pi n_{eff}L_{cav}}.$$

Then, applying Eq. (1.9), one gets:

$$\mathcal{F} = \pi \frac{\alpha_r |\tau|}{1 - \alpha_r^2 |\tau|^2} \tag{2.22}$$

and

$$\mathcal{F} = \frac{\pi}{1 - |\tau|^2} = \frac{\pi}{|\eta|^2} \quad \text{when} \quad \alpha_r = |\tau| \approx 1.$$

for the Finesse in the two cases.

Finally, the Quality factor, given by Eq. (1.13), becomes:

$$Q = \frac{\lambda}{\Delta\lambda_{3dB}} = \pi \frac{n_{eff} L_{cav}}{\lambda} \frac{\alpha_r |\tau|}{1 - \alpha_r^2 |\tau|^2} = \frac{n_{eff} L_{cav}}{\lambda} \mathcal{F} \tag{2.23}$$

and, when $\alpha_r = |\tau| \approx 1$, it can be written as:

$$Q = \frac{\pi n_{eff} L_{cav}}{\lambda |\eta|^2}.$$

Coupling with the second waveguide

In our case the resonator is also coupled to a second waveguide (see Figure 2.6). From the point of view of the original waveguide, the presence of the second (lower) waveguide merely modifies the internal loss parameter from α_r to $\alpha_r |\tau_2|$ (the 1 and 2 subscripts now refer to the "In-Through" and "Drop-Add" waveguides, respectively). All the expressions given above apply, provided we set $\tau \rightarrow \tau_1$ ($\eta \rightarrow \eta_1$) and $\alpha_r \rightarrow \alpha_r |\tau_2|$. The output power $|a_d|^2$ from the second guide, i.e. from the Drop-port, is of special interest. At resonance

$$|a_d|^2 = \frac{(1 - |\tau_1|^2)(1 - |\tau_2|^2)\alpha_r}{(1 - \alpha_r |\tau_1 \tau_2|)^2}. \tag{2.24}$$

Full transfer of power from the input guide to the output guide, i.e. $|a_d|^2 = 1$, occurs when the two following conditions are satisfied: $\alpha_r = 1$ (negligible internal losses) and $|\tau_1| = |\tau_2|$ (identical coupling). The transfer of power between waveguides can thus be controlled by small changes in $|\tau_1|$ or $|\tau_2|$.

2.2 Numerical Simulations

As a conclusion of this chapter this section gives a survey of the two numerical methods used in our work: Finite Difference Time Domain (FDTD) and Finite Element Method (FEM). We will show only one example of each method without explaining how them works since they are well known. However for a treatment of both approaches see [35].

2.2.1 FDTD

Since is a time domain approach, its main advantage is the possibility to describe, in addition to steady state behaviour, also the transition one. The particular 3-D FDTD simulator used in this work is explained in [36].

Case of study

Here we report some results as an application example of the simulator. The reference taken to test the FDTD method is a SOI technology based racetrack microring resonator [37]. In Figure 2.7 both the device layout and geometrical parameters definitions are reported.

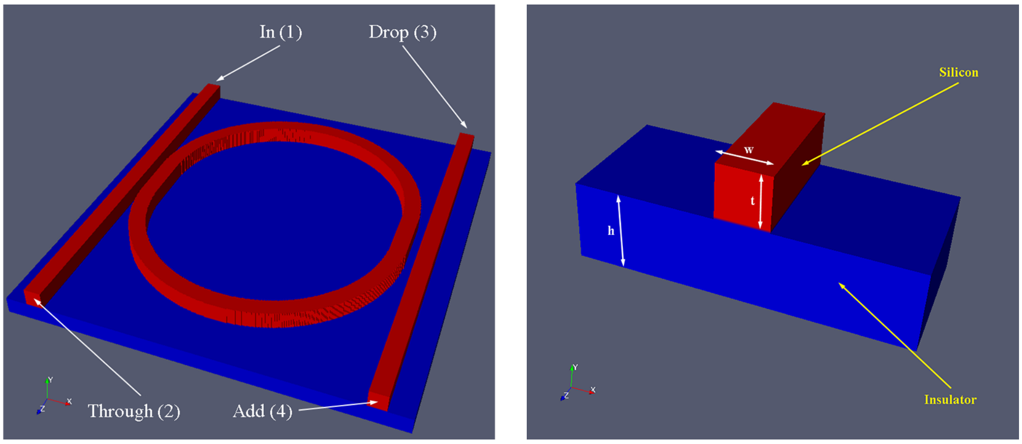

(a) (b)

Figure 2.7: *Racetrack ring resonator under test. (a) Device layout and port displacement. (b) Parameters of the SOI technology used.*

In Table 2.2 the values of such parameters are reported at $\lambda = 1550$ nm.

Simulation Results

In Figure 2.8a the main field component distribution, E_y i.e. TM polarised, is reported in the resonance state while Figure 2.8b shows the time evolutions of E_y at the ports. Note that after about 6 ps the device response is stable.

In Table 2.3 the fundamental parameters values of the resonator are reported. This parameters where calculated using a curve fitting based on a lorentzian function [38].

Finally both transfer functions between In-port and Through-port, and between In-port and Drop-port are plotted in Figure 2.9.

Parameter description	Parameter name	Value
Silicon refractive index	n_f	3.4
Silicon dioxide refractive index	n_c	1.6
Waveguides width	w	0.4 µm
Film layer thickness	t	0.4 µm
Cladding layer thickness	h	0.4 µm
Gap between the ring and the bus-bars	g	0.2 µm
Coupling length	$L_{c\eta}$	1.0 µm
Ring radius	R	3.0 µm

Table 2.2: *Technological and geometrical parameters of the DUT.*

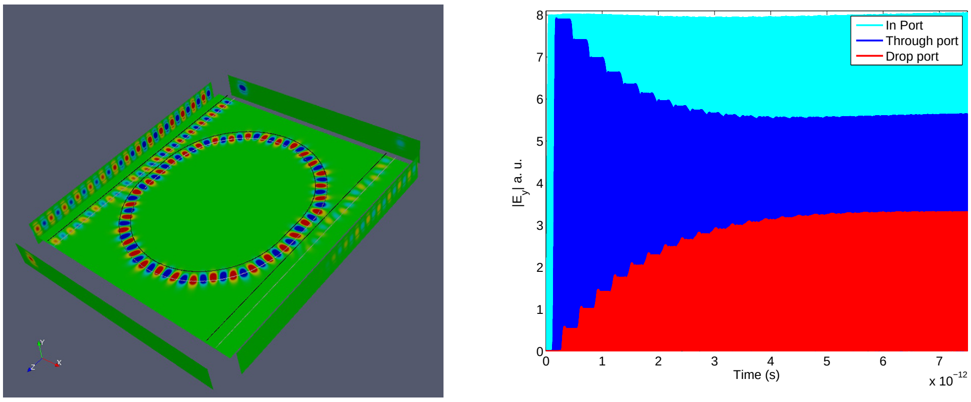

(a) (b)

Figure 2.8: *Racetrack simulation results. (a) Continuos wave simulation near resonance of 1550 nm.(b) Time evolution of the main field component E_y of the three principal device ports.*

Name	Value
λ	1550.41 nm
FSR	27.106 nm
Q	1482
$\mathcal{F}$	26
ER	-4.8403 dB

Table 2.3: *Racetrack fundamental parameters computed around resonance.*

Now, through this example FDTD has demonstrated its potential. In fact, after a unique simulation we get all the parameters and the data necessary. However, as will be clearer in §5.1, the geometrical parameters values chosen for our res-

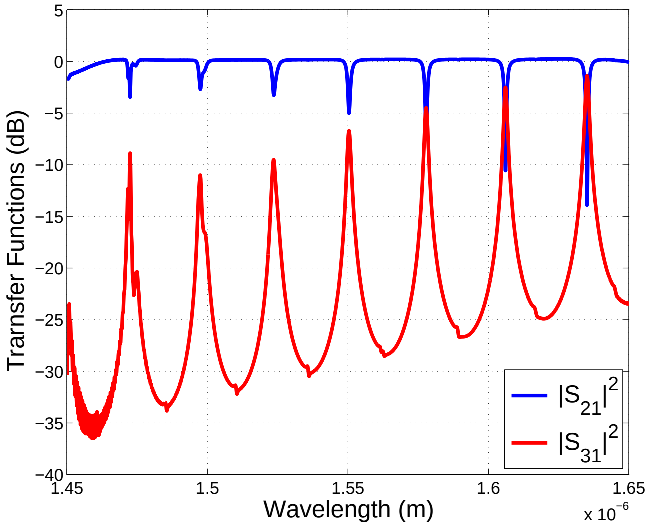

Figure 2.9: *Through-port and Drop-port transfer functions. Port indexing refer to Figure 2.7*a

onators are such that the final device dimensions are too large to let us to simulate them with FDTD.

2.2.2 FEM

The FEM solver used in this work is a commercial software called COMSOL Multiphysics. The simulations performed have the aim to check if the approximations taken for the refractive indices distributions , taken during both the analysis and the design processes, are reasonable (see §5.1).

We will show two mode computation examples applied to another case study [39]. This particular example is chosen because the substrate is Lithium Niobate and the geometry dimensions are closer to our fabricated device ones, then those of SOI technology.

The ridge technological process showed in [39] is based on a selective etching of the crystal via PE and then a waveguide fabrication through Titanium diffusion. This technology is different from our approach completely based on ion-implantation, but is useful to focalise the kind of devices we are going to design, fabricate and characterise in the next chapters.

So, in Figure 2.10 is reported the fundamental mode of the Ti:LiNbO$_3$ ridge waveguide described in [39].

Figure 2.11 shows the fundamental mode of the same waveguide with a bend radius $R = 200$ µm. Note how the maximum of the mode distribution is near the

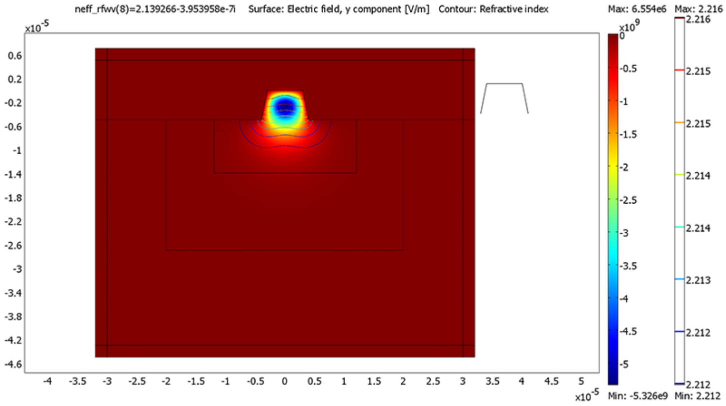

Figure 2.10: *Mode profile of a Ti:LiNbO$_3$ ridge waveguide. Contour plot indicates the refractive index distribution.*

outer rim. This is a case of whispering gallery mode i.e. guided only by the outer rim not by the waveguide anymore [31].

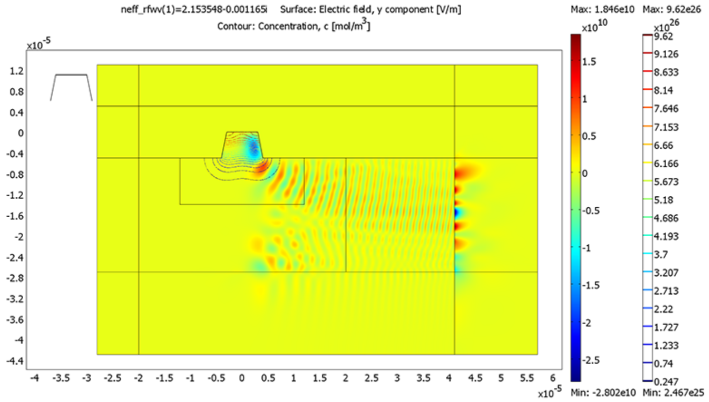

Figure 2.11: *Mode profile of a bent Ti:LiNbO$_3$ ridge waveguide with $R = 200\ \mu m$. Contour plot indicates the Titanium concentration profile.*

This result was obtained applying in COMSOL the conformal mapping method to simulate the bending structure [27]. So thanks to its versatility the FEM solver allows us to completely characterise the theoretical mode distribution of the modes that propagate in the structure. This approach will be widely used in §5.1.

Chapter 3

Lithium Niobate

In this chapter we will focus our attention on the substrate used in this work: Lithium Niobate ($LiNbO_3$) and its optical characteristics modification through ion-implantation processes.

Lithium Niobate (LN), i.e. Lithium and Niobium Oxide, is a birefringent hexagonal crystal with a wide transparency from 340 nm to 4600 nm [40].

The atomic arrangement within the stoichiometric hexagonal unit cell, as shown in Figure 3.1a, consists of six $LiNbO_3$ with Li (small light grey spheres) and Nb (small dark grey spheres) ions located on the polar c-axis (crystal axis also indicated with z) and the O (large dark grey spheres) atoms in general positions (Figure 3.1b).

Li occupies an oxygen atom octahedron that shares faces with adjacent similar octahedra on either side along the trigonal axis. One such octahedron is empty, the other is occupied by Nb. The triple octahedron is repeated, with alternating sequences having identical orientation, along the polar axis (Figure 3.1c). The spacing between corresponding atoms in alternate sequences forms the c-axis repeat [1].

Note that this particular distribution of the three ionic species forms electric dipoles and so, below a certain temperature, i.e. *Curie Temperature* (∼ 1142 °C [40]), LN is ferroelectric [42]. So it possess a so-called spontaneous electric polarisation.

Other important physical properties due to its crystal structure are: pyroelectricity, piezoelectricity, thermo-opticity and, most important for us, electro-opticity.

Thus, in the next section we will describe its intrinsic optical characteristics. Then we will proceed explaining how ion-implantation can be used to change both optical and chemical characteristics of LN.

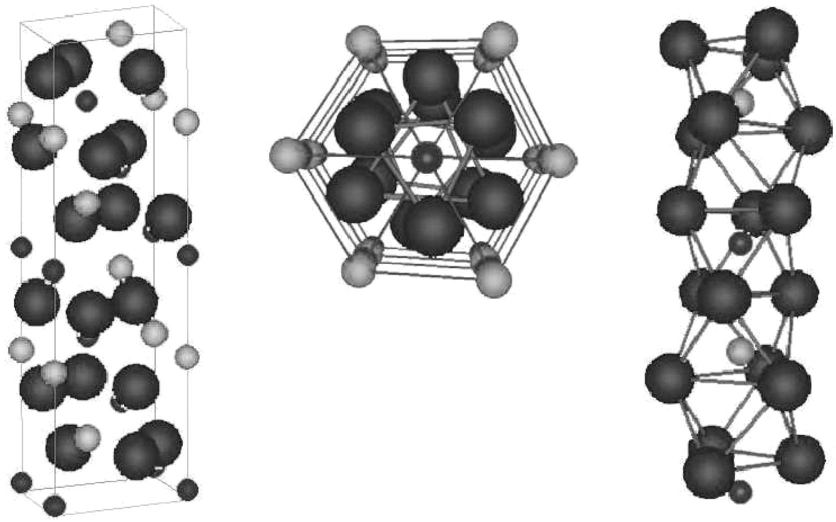
(a) (b) (c)

Figure 3.1: *Lithium Niobate crystal cell [41]. (a) Vertical view of a conventional cell. (b) C-axis view. (c) Oxygen atom octahedron structure with Li and Nb alternatively.*

3.1 Optical Characteristics

As pointed out before, $LiNbO_3$ is an anisotropic uniaxial crystal [43]. Its extraordinary and ordinary refractive index dispersions, described by two different *Sellmeier equations*, are plotted in Figure 3.2a with the coefficients reported in [40]. Since $n_o > n_e$ LN is called a “negative” crystal (being ”positive” crystals those with $n_o < n_e$).

Some examples of $LiNbO_3$ wafers are reported in Figure 3.2b. Depending on which of the three crystal axes is perpendicular to the wafer plane they are called *x*, *y* or *z-cut*.

The values of the electro-optic tensor, $\bar{\mathbf{r}}$, are given in Table 3.1 in two different conditions based on the value of the applied electric field frequency: unclamped ($f < 500\,\mathrm{kHz}$) and clamped ($f > 10\,\mathrm{MHz}$), for further details about this behaviour see [1].

	r_{13}	r_{22}	r_{33}	r_{51}	r_z
unclamped	10	7	33	33	18
clamped	9	3	31	28	19

Table 3.1: *LN electro-optic coefficients (pm/V at* $\lambda = 633$ *nm).*

Now we can proceed describing the core of this work: ion-implanted Lithium

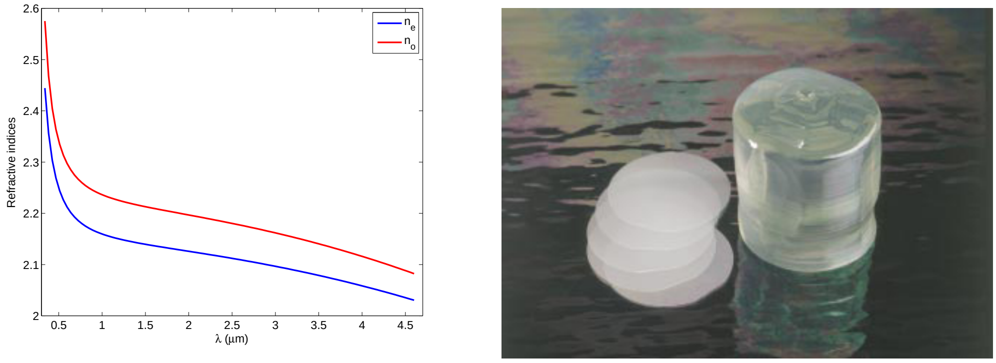

(a) (b)

Figure 3.2: *Lithium Niobate optical properties and aspect [40]. (a) Sellmeier dispersion curves at room temperature (27 °C). (b) Four inches wafers after crystal growth. Depending on which of the three crystal axes is perpendicular to the wafer plane they are called x, y or z-cut*

Niobate. We will start with a brief description of the physical principles of charged particles travelling through solids.

3.2 Ion Implantation effects

The specific energy loss of an ion through a solid material is called *stopping power* and can be written as sum of different parts:

$$\left[-\frac{dE}{dx}\right]_{tot} = \left[-\frac{dE}{dx}\right]_{n} + \left[-\frac{dE}{dx}\right]_{e} \tag{3.1}$$

here E is the energy and x is the coordinate along the travelling direction.

The first term of Eq. (3.1) represents the nuclear stopping power and the second the electronic one. The nuclear stopping power is caused by a sequence of elastic collisions statistically independent between the incident particle and the lattice atoms. It is the predominant term at low velocities [44].

At high velocities prevails the electronic stopping power. This effect is due to inelastic collisions between electrons in the medium and the ion moving through it.

Finally, when an ion travels through a solid with a velocity close to the one of its outer orbitals electrons, it has an high probability both to lose electrons to the target and to capture target electrons. This charge exchange process can contribute to the total stopping power [44].

In a crystal, if the ion travelling direction is close to a crystallographic axis or a low index crystallographic plane [42], one has to take into account the lattice periodicity. In this case, in fact, the particle is deflected by a series of collisions with the axial or planar channel walls. For this reason this phenomenon is so-called *channelling*. If an ion is channelled by the crystal lattice, it has a much larger penetration than a random incident one.

This effect will bring about undesirable problems when one wishes to have accurate control of the implanted ion profiles in the crystal. In practice, the ion beams are tilted at a slight angle (for example, $\sim 7°$) from the sample surface normal planes for implantation into $LiNbO_3$ crystals, by which the channelling effect can be minimised.

Implanters, tandem accelerators, and so on are used to generate energetic beams of both light and heavy ions. As described above, the incident ions lose their energy mainly through electronic and nuclear energy-transferring mechanisms. The ions, implanted at different stopping powers determined by the ion mass, energy, and target materials, will cause damage through these two mechanisms [45].

More in details, the damage generated by the nuclear scattering of the incident ion with the target atoms, is so-called nuclear damage and is correlated with the nuclear stopping power introduced before.

Besides this kind of damage, it is known that the dense excitation of the electronic sub-system, generated in a nanometre region surrounding the ion path, can be partly converted into lattice damage so-called electronic damage [54].

Moreover, when an electronic stopping power threshold, dependent on the ion velocity, is exceeded an amorphous track is directly generated by the ion passage (for an application of this phenomenon see [46]).

Otherwise multiple ion trajectories overlapping are necessary to accumulate a critical concentration of defects to induce a local lattice collapse. So far it has been demonstrated that defects produced by electronic and nuclear processes are different, as they produce a different response in multi-axial *Rutherford Backscattering Spectrometry-channeling* (RBS-C) experiments [47].

High-fluence (normally above 10^{16} ions/cm^2) light ions, typically referring to H or He particles, at energies of several keV to MeV induce a nuclear damage layer buried inside $LiNbO_3$ crystals.

Middle-light-mass ions such as C, N, O, F, Si, Cl, Ni, or Cu at energies of several MeV, can cause relatively strong modifications in the implanted regions in $LiNbO_3$ even at lower fluences of 10^{14} ions/cm^2 [48]. In these cases, the electronic stopping powers are much higher than those of light ions. Nevertheless, low-fluence heavy-ion-induced lattice disorders can also be removed by suitable thermal annealing (200–300 °C).

Figure 3.3 shows the distributions of the electronic and nuclear energy deposition (i.e. the opposite of the stopping power) of 2 MeV He and 6 MeV O ions implanted into $LiNbO_3$ crystals from numerical simulations of SRIM (Stopping and Ranges of Ions in Matter [49]).

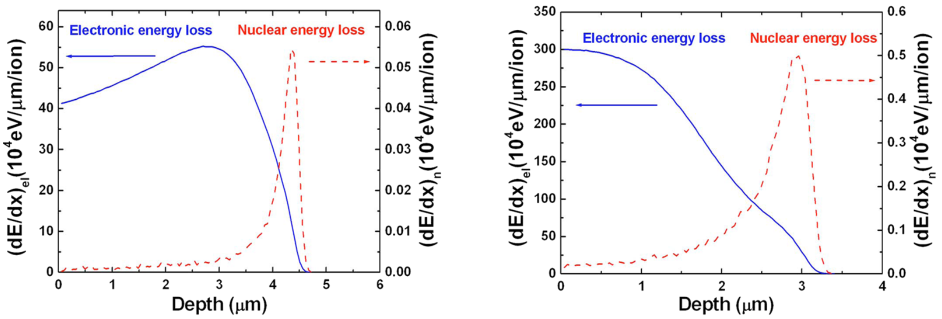

(a) (b)

Figure 3.3: *Distributions of electronic (solid lines) and nuclear (dashed lines) energy deposition of (a) 2 MeV He and (b) 6 MeV O ion implanted into LN crystals calculated by SRIM 2006.*

For the purpose of photonic applications, ion implantation has proven to be an efficient method for fabricating optical waveguide structures in many materials due to its accurate control of the refractive indices of the substrates. In fact, in some crystals with low phase transition temperatures or very stable chemical properties, ion implantation is one of the most effective techniques to guide structures within them [45].

$LiNbO_3$ waveguides produced by the implantation of light and heavy (medium-mass) ion beams have been realised for many years and exhibit attractive properties for various photonic applications [1].

Now, we will describe two different uses of ion-implantation. The former changes the refractive index profile in the vertical direction and will be discussed in the next subsection. The latter allows the fabrication of ridge waveguides and so provides lateral confinement. It will be explained in §3.2.2.

3.2.1 Refractive Index Tailoring

As pointed out before, for low particle velocities, the stopping power which prevails and determines the damage profile inside the crystal is the nuclear one.

Figure 3.4 shows a defective phase diagram (N^* is the defect fraction as measured by RBS-channeling) obtained following a predictive model based both on empirical formulae and SRIM simulations described in [50].

The plot area is divided into two main regions, one dominated by nuclear damage ($N^*_{nuc,x} > N^*_{el}$) and the other dominated by the damage induced by electronic

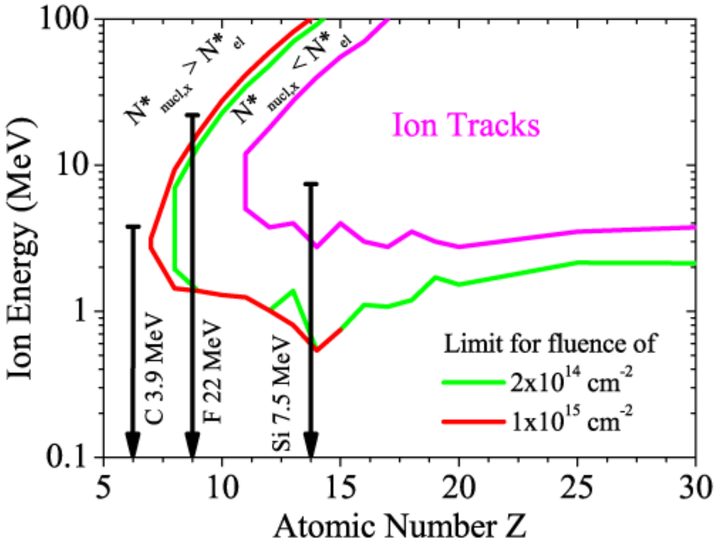

Figure 3.4: *Defective phase diagram of ion-implanted LN for two different fluences.*

excitation ($N^*_{nuc,x} < N^*_{el}$). Note that the border line depends on the irradiation fluence.

The electronic damage region is further divided into two regions characterized by sub-threshold damage and ion tracks (i.e. amorphous tracks as described in §3.2). For a selected ion of a given energy it is possible to qualitatively predict the main features of the damage generated by the energy loss into the LN sample [51].

Of the three examples shown in the Figure 3.4, only 3.9 MeV carbon ions produce nuclear damage with negligible electronic one. In fact its arrow (i.e. its energy decreasing) doesn't cross the electronic damage region nor the one of ion tracks. In this case, it is possible to apply our refractive index variation model [52] based both on SRIM simulations and m-lines measurements (see §5.2.1).

The model results are reported in Figure 3.5 where the two refractive indices distributions are expressed in function of E_d, a normalisation parameter used to correlate the results of different implantation processes. It is the product of the energy transferred to the target atoms S_n (i.e. the nuclear stopping power computed by the SRIM program) and the ion fluence Φ:

$$E_d = S_n \times \Phi.$$

These two distributions are the best fit curves of literature data normalised to E_d and represents the state of the art available at the beginning of the present work.

Note that n_e goes above the bulk value (i.e. of virgin LN), n_{ev}, while n_o remains

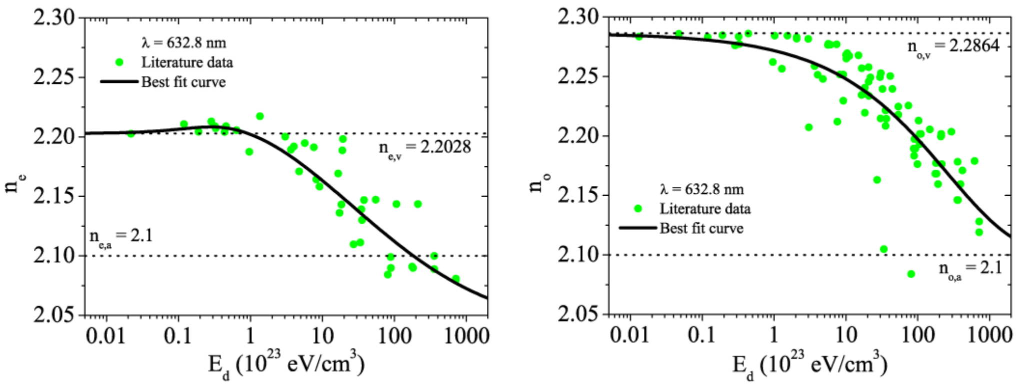

(a) (b)

Figure 3.5: *Refractive index tailoring in Lithium Niobate by ion implantation. Best fit curves of literature data of (a) n_e and (b) n_o distributions in function of E_d [52].*

always under n_{ov}. The reason of these two different trends could be ascribed to the three contributions to the indices change induced by nuclear damage: volume, polarisability and spontaneous polarisation variations [42].

In fact the specific volume of LN increases with damage and this causes both n_o and n_e to decrease. On the other hand ion bombardment locally breaks crystal order causing the reduction of LN anisotropy and consequently varying the polarisability and the spontaneous polarisation. This latter in particular decreases when damage increases leading n_o and n_e to converge (decrease of n_o, increase of n_e) towards a common value when polarisation becomes zero.

So n_o has two contributions which push its value down when damage increases while n_e has a volume contribution which pushes its value down and one due to spontaneous polarisation which pushes its value up when damage increases. This last contribution seems to prevail at medium-low damage while the volume one is prevailing at high damage [52].

Therefore, an ion-implanted waveguide sustains extraordinary polarised modes with almost no intrinsic loesses while the ordinary ones are lossy. So, typically after some mm of propagation through the waveguide, the contribution of ordinary polarised modes to the output power is negligible and the light results polarised along the extraordinary axis.

The two curves of Figure 3.5 have to be in the following way. First we choose the ion (i.e. Carbon for the reasons described before) and then an implantation energy which settles the depth of the ion barrier. Now the only free parameter remained becomes the fluence which, at this point, determines the refractive index profile.

3.2.2 Etching Rate alteration

Before introducing how ion-implantation changes the LN etching properties we have to explain how bulk $LiNbO_3$ is etched.

Chemical etching in aqueous hydrofluoric solution of Lithium Niobate works as following [53]. At first, the negatively charged free bonds of oxygen atoms at the surface are saturated with H^+ ions very rapidly by electrostatic attraction.

Then the oxygen can desorb from the surface in the shape of an OH^- molecule or as H_2O after a further complex formation by another H^+ ion. In a second step, the metallic (Li and Nb) atoms can be removed by an attack from either HF or HF_2^-, leaving behind free oxygen bonds at the new surface and the process restart.

This kind of "slice" etching has a negligible rate in virgin Lithium Niobate but, since it depends on the number of oxygen free bonds, increases with the lattice damage.

For this reason heavily damaged layers were produced in LN by using different ion implantation parameters. For each condition, defects were generated in the surface layer by a specific dominant energy release process, i.e. nuclear or electronic. The chemical etching properties of the irradiated areas were then correlated to the damage level evaluated by RBS-C [54].

Moreover, combining both electronic and nuclear damage to get the maximum defect fraction possible ($N^* \approx 1$) the etching rate was increased by 100 times compared to that of bulk $LiNbO_3$ [50].

In Figure 3.6a are reported three defect fractions for different fluences in the case of 4 MeV Cu ion implanted in Lithium Niobate. Figure 3.6b shows the etching profile for the best case: 1×10^{15} ions/cm^2. Note that the amorphous layer extension goes from the surface to the depth settled by the implantation energy.

So using a masking layer it's possible to modify LN through this particular ion-implantation recipe and one obtains very smooth sidewalls as shown in Figure 3.7. Note that the ridge shape is limited only by the particular photolithography used as it will be clearer in the next chapter.

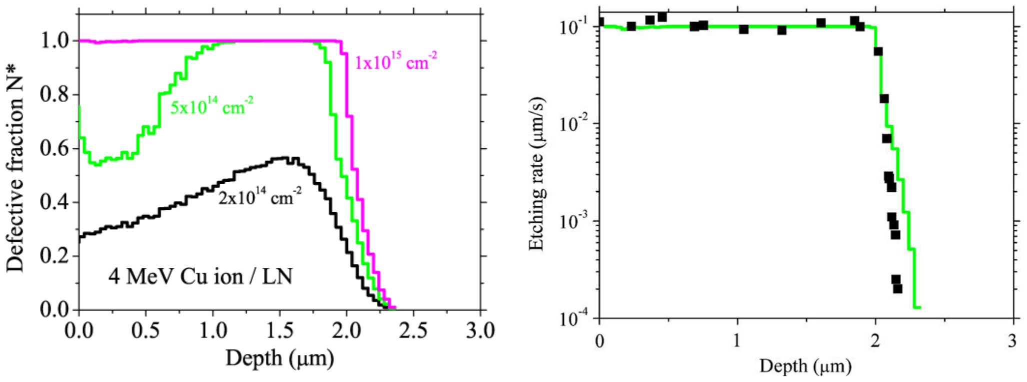

(a) (b)

Figure 3.6: *Etching Rate alteration. (a) Total defective fraction produced by 4 MeV Cu ion implantation in LN for three different fluences. (b) Measured (squares) and simulated (line) etching rate depth profile for a LN sample implanted with 4 MeV Cu ion at the fluence of* 1×10^{15} *ions/cm*^{2}.

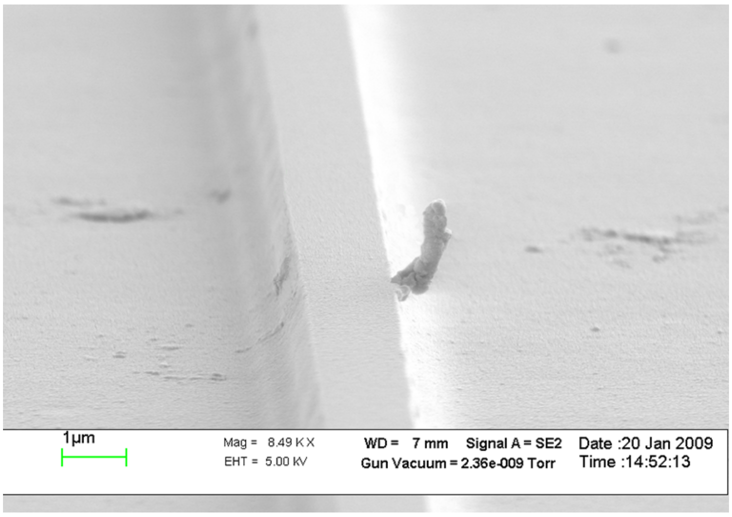

Figure 3.7: *SEM image of a micrometric edge channel waveguide fabricated by ion implantation/etching process. The height of the lateral walls is about 1.4 μm.*

Chapter 4

Design and Fabrication

This chapter has a double aim. The first one is to show the design of our devices following a standard procedure consolidated in forty years of technological expertise achieved by the staff of CNR-IMM Laboratories in Bologna.

Secondly a brief documentation of our technological run, which is still under development, will be given to permit a better understanding of the problems encountered during the fabrication of our prototypes and the solutions proposed in §5.5.

Even if the technology commonly used at CNR-IMM is well know for Silicon, it is not the same for $LiNbO_3$ crystals since this material has a lot of physical properties that have to be taken into account (see §5.3).

4.1 Project

We will start describing some general features of our devices starting from the ones imposed by our technology.

The first limiting factor is the minimum feature size allowed by the photolithographic process used, which is directly correlated with the working wavelength of the mask aligner UV lamp. In our case the minimum allowable feature size is ~ 1 μm.

As shown in Figure 2.1b the minimum feature size in fabricated SOI devices is usually ~ 100 nm, thanks to the use of the *e-beam* lithography. In our case, we used a hard-contact lithography which permits to obtain device dimensions in the range of hundreds of microns, with the exact values computed in §5.1.

Another important feature of our devices is the ridge technology. In fact, thanks to the strong lateral confinement provided by the surrounding medium, i.e. air [25], ridge waveguides allow small bending radii (~ 100 μm) compared to embedded waveguides fabricated through PE or Ti-diffusion.

Moreover, as pointed out in §3.2.1, our waveguide is an intrinsic polariser, thanks to ion-implantation. Therefore, since the only polarisation guided is the extraordinary one, and our devices are ring-based, to maintain the isotropy on the propagation plane avoiding polarisation crosstalk [3], the wafer type chosen is z-cut and so the polarisation guided will be the TM one.

The last general feature of our device, is the presence of electrodes to permit the tuning of the resonance frequency of the ring by the electro-optic effect.

4.2 Mask Design

So two photolithographic masks were designed using the commercial software tool CADENCE. One mask is for the devices, while the other one is for the electrodes. Figure 4.1a shows the layout for a resonator. The red layer represents the rings mask fabricated for negative photoresist, while the green one is the electrodes mask designed for positive photoresist.

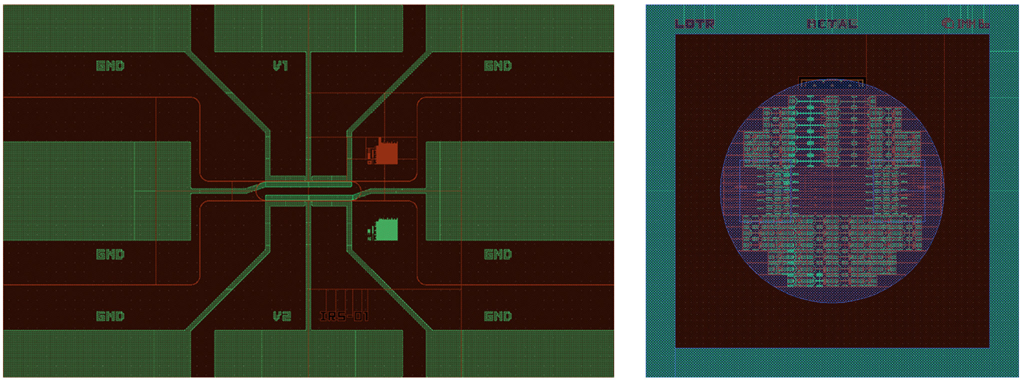

(a) (b)

Figure 4.1: *Mask Design. (a) Device example with two mask layers and (b) final layout of the mask set.*

The photoresist tone is not an accidental choice. In fact, the negative photoresist commonly used at IMM of Bologna (ma-N 1420) is the best choice to fabricate ridge waveguides, since it has more stopping power compared to the positive photoresist (HPR 504). In other words: ma-N allows us to fabricate a deeper ridge than the one obtained using HPR.

Instead the positive photoresist was chosen for the electrodes layer because its higher reliability.

The complete layout of the final photomask is reported in Figure 4.1b. The masks are fabricated on a soda-lime quartz substrate by an external company and have a lateral dimension of five inches. Note that the wafer is plotted in a superimposed reference layer colored in blue and has a diameter of three inches.

4.3 Technological Run

In this section we will illustrate the technological procedure followed to fabricate the first prototypes of optical microring resonators based on ion-implanted $LiNbO_3$ ridge waveguides.

Even if many of the fourteen technological steps, taken during the devices fabrication, are commonly used and well known from Electronics [55], their application to LN crystals has to be performed appropriately.

4.3.1 Planar Waveguide

The first main step consists in the manufacturing of the surface planar waveguide for the vertical confinement of the light. Before performing this step a 100 nm thick film of Cr is evaporated onto the LN wafer. This is necessary to avoid the electrostatic charge accumulation on the crystal surface during ion-implantation which makes the wafer break (see Figure 4.2a). The Chrome will be used also as adhesion layer for the photoresist in the next step.

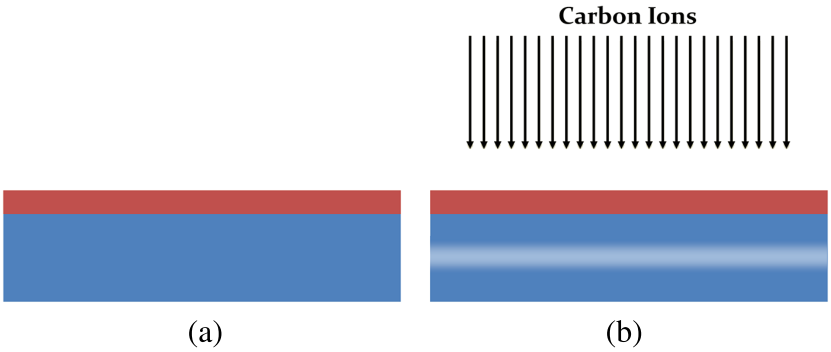

(a) (b)

Figure 4.2: *Planar waveguide manufacturing. (a) LN z-cut wafer (colored in blue) with a 100 nm evaporated layer of Cr (colored in dark red). (b) Planar waveguide formation by Carbon ions implantation (the lighter regions inside the crystal indicate the C ions barrier).*

Then the planar waveguide is obtained by implanting the whole LN wafer with 3.9 MeV C ions at a fluence of 4×10^{14} ions/cm^2 followed by annealing in O_2 atmosphere at 280 °C for 2 hours (see Figure 4.2b).

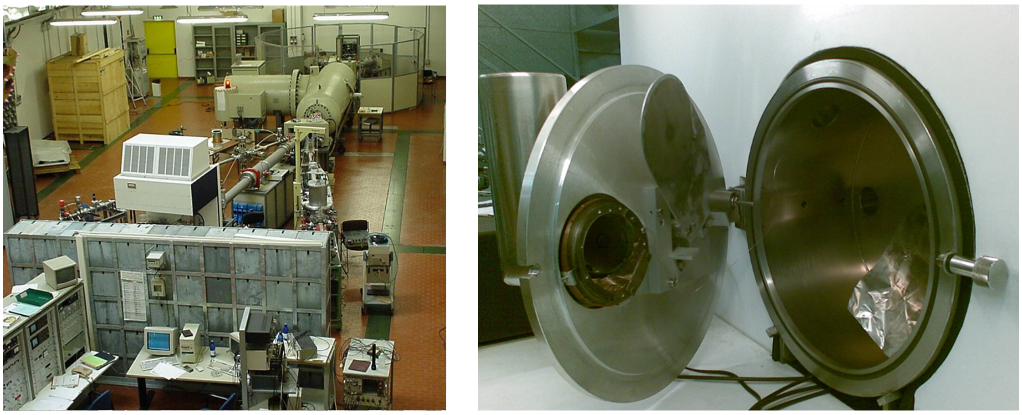

(a) (b)

Figure 4.3: *Ion Implantation. (a) 1.7 MV High Voltage Engineering Tandetron 4117HC and (b) our sample mounted on the tilted holder.*

C ions were chosen because they produce the desired refractive index profile (see §5.2) at a moderate fluence, without generating measurable electronic damage in the guiding region (see §3.2.1).

Figure 4.3a shows the Tandetron 4117HC high voltage accelerator available at CNR-IMM Laboratories in Bologna and Figure 4.3b displays a three inches *z-cut* wafer mounted inside the vacuum chamber. Note the tilted holder to avoid channelling (see §3.2).

4.3.2 Ridge Manufacturing

The definition of our ridge structures, as pointed in §4.2, is performed using as masking layer a 2 μm thick negative PR layer, deposited onto the thin Cr adhesion film and patterned by conventional photolithographic techniques (see Figure 4.4).

Then the Cr adhesion layer is defined through wet etching using the following solution: $[Ce(SO_4)_2\ H_2O]:H_2O:H_2SO_4$ with ratio 50 g :500 cc : 25 cc (see Figure 4.5a). Before the second ion-implantation step, i.e. the amorphising one, a thin Gold layer is sputtered to avoid charge accumulation on the crystal surface (see Figure 4.5b).

The maximum Cu energy that can be completely absorbed by this PR layer is 1 MeV, corresponding to an amorphised LN depth of 0.7 μm at a fluence of 1×10^{15} ions/cm^2 (see §3.2.2). In order to obtain an efficient lateral light confinement, a ridge deeper than 1 μm is required (see §5.1), therefore we need to perform two implantation/etching steps.

So after the first Cu implantation the Au film is removed through wet etch-

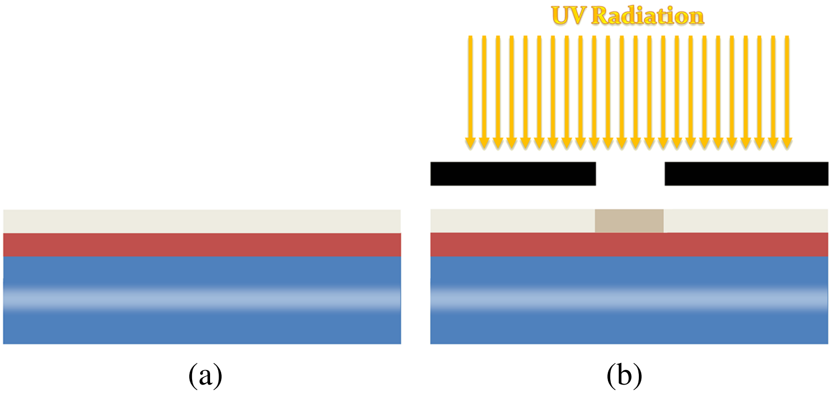

Figure 4.4: *Two steps of the negative photoresist patterning (colored in grey): (a) PR spinning and (b) PR exposition (since it is negative it solvent resistance increases with illumination an so is colored with a darker grey).*

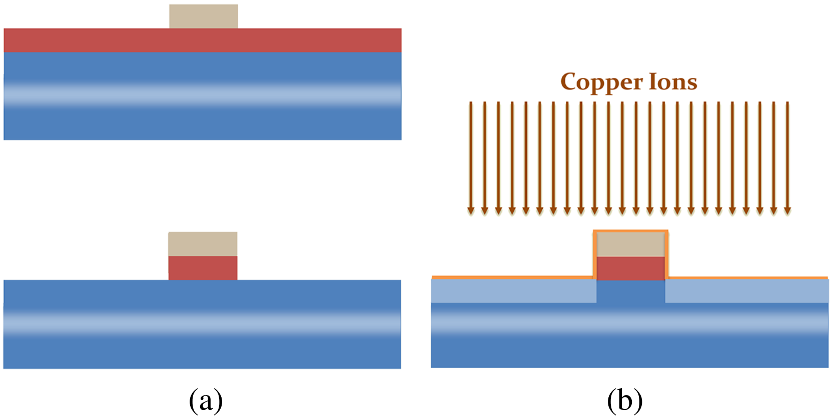

Figure 4.5: *Ridge waveguide fabrication 1/2. (a) Cr wet etching and (b) LN amorphisation trough Cu ions implantation (amorphised regions colored in light blue).*

ing using the following solution: KI:I_2:H_2O with ratio 100 g :30 g : 475 cc. Then the HF etching in 49% aqueous solution is performed to remove the amorphised $LiNbO_3$. The etch time is 60 sec.

Another cycle of Gold sputtering, Cu ions implantation and wet etching of both Gold and LN is taken. Finally the Cr layer and the carbonised PR are removed through a Chrome wet etching at 70 °C (see Figure 4.6a). The final result is shown in Figure 4.6b.

In Figure 4.7 is reported the top view of the same device detail after the photolithographic process and after the ridge fabrication through etching rate alter-

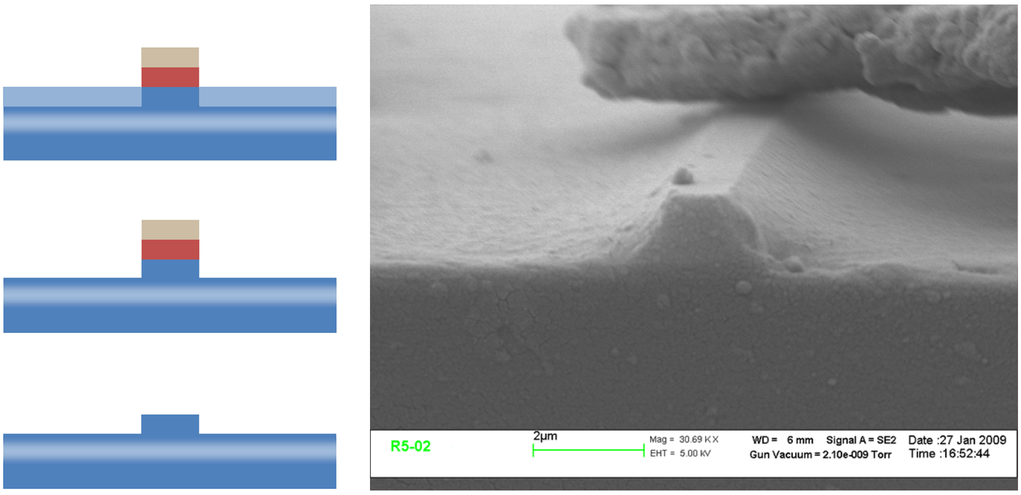

(a) (b)

Figure 4.6: *Ridge waveguide fabrication 2/2. (a) Amorphised LN removed through HF etching. (b) SEM image of the vertical section of a ridge waveguide.*

ation (see §3.2.2).

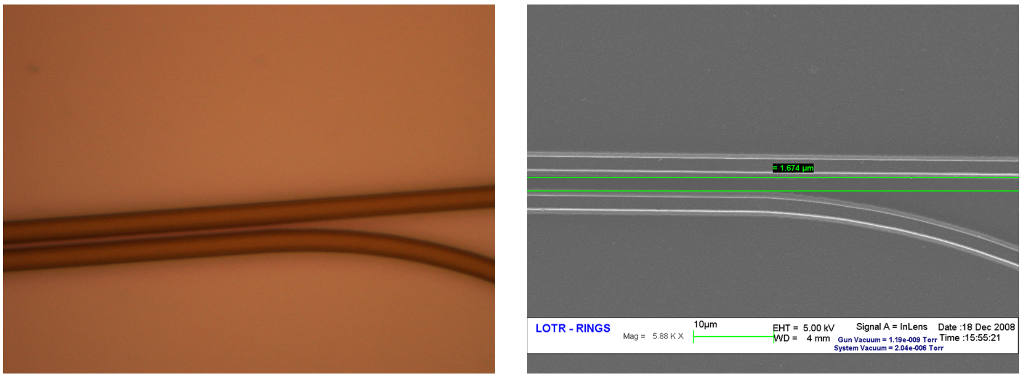

(a) (b)

Figure 4.7: *Rings resonators patterning. (a) Optical microscope image of negative photoresist patterned at the end of the photolithographic process. (b) SEM image of the same device portion at the end of the ridge fabrication process.*

4.3.3 Electrodes fabrication

In order to avoid losses due to plasmon effects [42], a 150 nm SiO_2 layer is evaporated on the wafer surface, after an accurate cleaning of the patterned crystal. Then an Aluminium layer thick 500 nm is evaporated and covered a by positive PR spun to get a thickness of 1.1 µm (see Figure 4.8a).

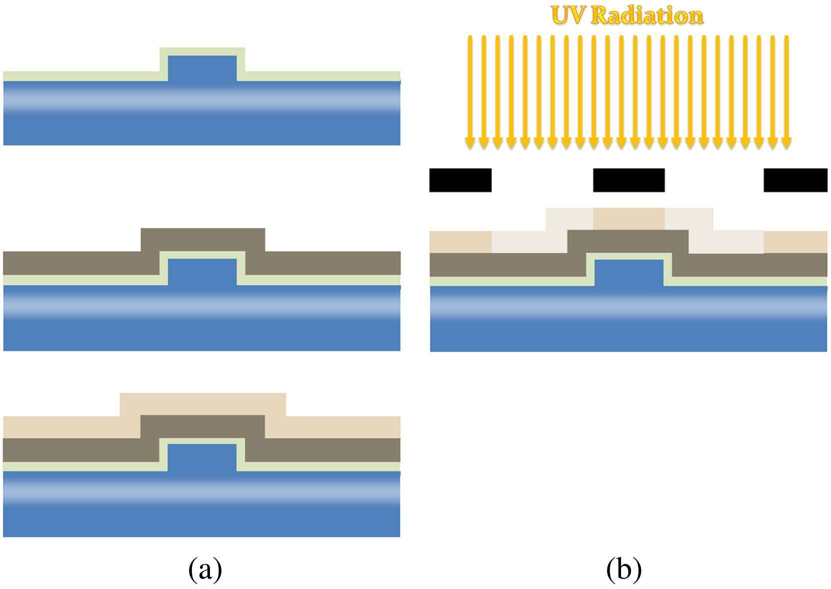

Figure 4.8: *Electrodes fabrication 1/2. (a) SiO_2 evaporation (green) and Al evaporation (dark grey). (b) PR (beige) exposition (since it is positive its solvent resistance decreases with illumination an so is colored with a lighter beige).*

So the PR is patterned by conventional photolithographic techniques (see Figure 4.8b). Then the electrodes layer is defined using a Reactive Ion Etching (RIE) system (see Figure 4.9a) and the masking PR layer is removed. The final result is shown in Figure 4.6b.

Figure 4.10 shows the final outcome of this procedure. In particular, Figure 4.10a displays the same part of Figure 4.7 for a different device. We can notice that here there is no gap: this is the first technological issue that has changed the theoretical device behaviour as will be clearer in §5.3.

Finally Figure 4.10b gives a view of the device core: the ring resonator coupled to two straight waveguides.

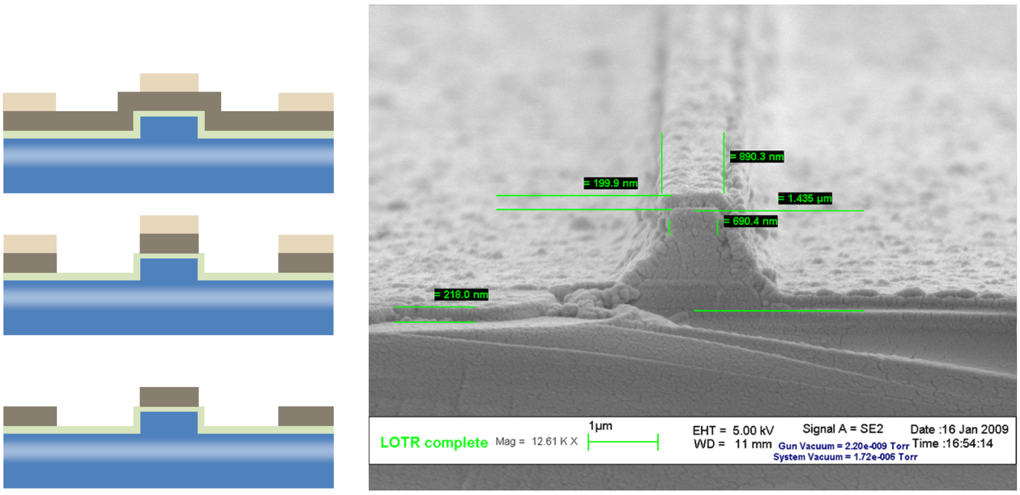

(a) (b)

Figure 4.9: *Electrodes fabrication 2/2. (a) Al removed through RIE. (b) SEM image of the vertical section of a ridge waveguide covered by* SiO_2.

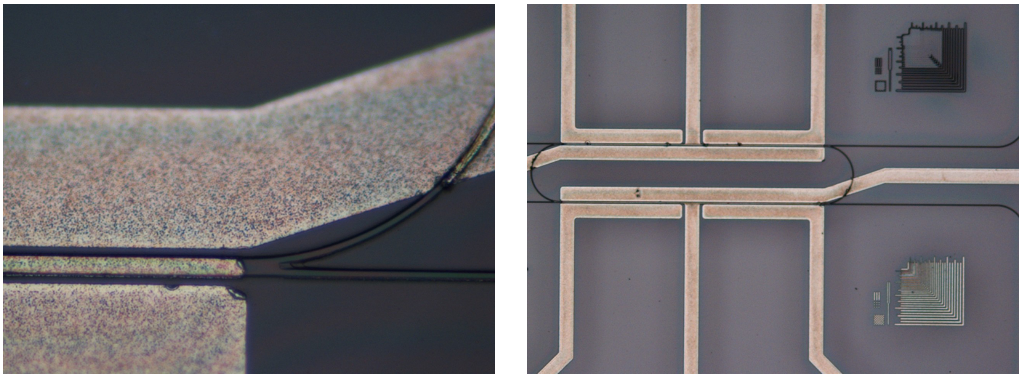

(a) (b)

Figure 4.10: *Optical Microring Resonators based on ion-implanted* $LiNbO_3$ *ridge waveguides. Optical microscope image of: (a) the coupling between the ring resonator and one of the two bus-bars, (b) the total device layout.*

4.3.4 Optical preparation

Then the eighty devices produced were separated with a dicing saw an lapped to prepare the surfaces for the optical characterisation. The lapping stage is one of the most important and needs a lot of care since we have to glue our devices to the tool shown in Figure 4.11a.

Finally it is inserted into the holder illustrated in Figures 4.11b and 4.11c with the two set of polishing plates. The whole process has a duration of about 4 hours

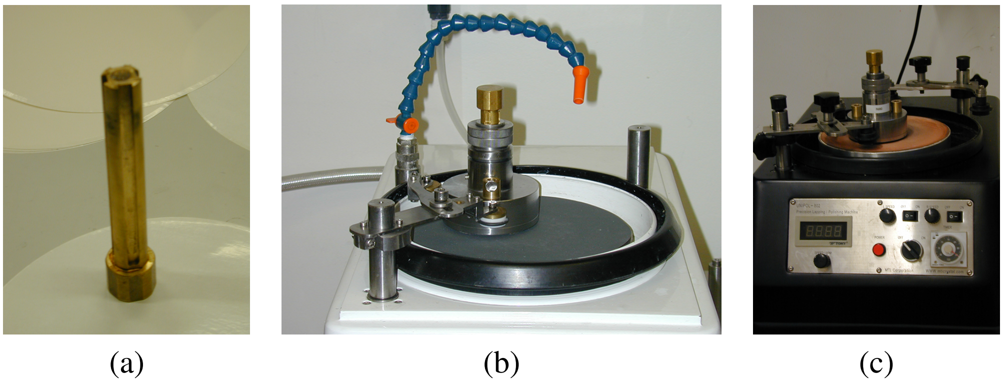
(a) (b) (c)

Figure 4.11: *Optical preparation: polishing & lapping. (a) Lapping tool: the devices are glued into the trenches. (b) Machine for surface preparation. (c) Machine for surface finishing.*

for each surface. After this procedure our device, ready to be characterised, is displayed in Figure 4.12.

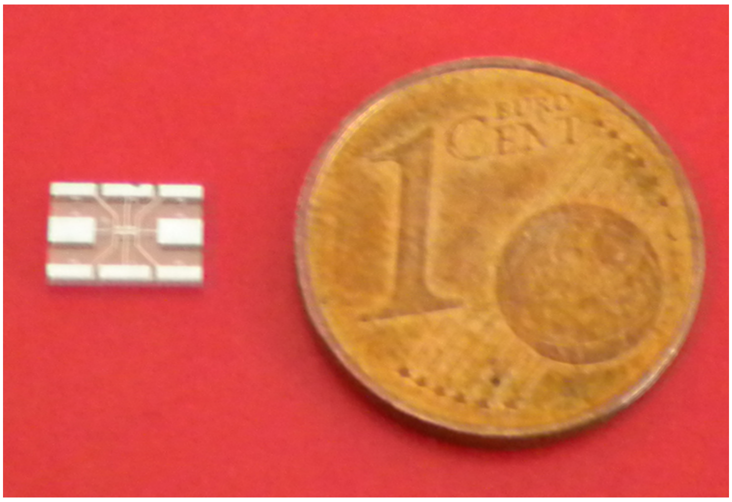

Figure 4.12: *Final device dimensions compared to an 1 € cent.*

Chapter 5

Results and Discussion

This chapter is a collection of all the results achieved in our work. We will start showing the design parameters computed using both the approaches illustrated in Chapter 2.

Then the issues, faced during the fabrication process shown in Chapter 4, will be analysed and a solution for each of them will be proposed.

Finally some characterisation results confirming the models introduced in §3.2.1 will be illustrated and commented.

5.1 Geometrical parameters computation

As mentioned in the introduction both the theoretical and the practical points of view were followed simultaneously. So, when we started the fabrication of our ring resonators, the refractive index profiles were not known as explained in §3.2.1. For this reason they were taken according to those of literature at the time [45].

In Figure 5.1 the two profiles computed for our routinely ion-implantation technological step: 3.9 MeV C ions at a fluence of 4×10^{14} ions/cm^2 followed by annealing (see §4.3.1) are reported. They were computed in the basis of the information available at the beginning of the present work.

Then we assumed, with a reasonable approximation [52], that both these profiles could be rescaled following Sellmeier index dispersions of virgin LN. So we choose, as working wavelength of our devices, $\lambda = 1500$ µm as this is the standard operation wavelength in optical systems.

Another issue concerns the ridge technology (based on etching rate alteration, see §3.2.2), that was still at an early stage, at the beginning of this work. It was supposed to be able to perform even three successive implantation/etching steps, i.e. a ridge height ~ 2.1 µm (see §4.3.2). For reasons explained in §5.3.2 these

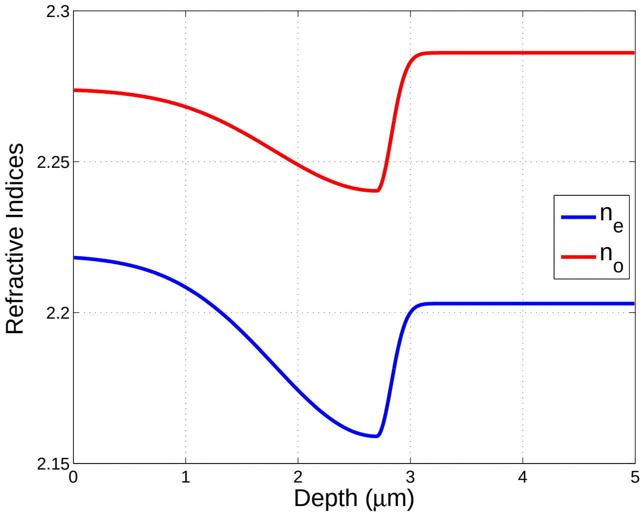

Figure 5.1: *Refractive index profiles of n_e and n_o at λ = 632.8 nm according with [45] for $LiNbO_3$ ion-implanted with 3.9 MeV C ions at a fluence of 4×10^{14} ions/cm^2 followed by annealing.*

steps were two instead, and so the obtained ridge height was ~ 1.4 μm.

After these considerations we can now show the design process of the geometrical parameters.

5.1.1 FEM modal simulations

To decide both the width, w, and the height, h, of the ridge waveguide several FEM simulations were performed. Concerning the height, since we need strong light confinement to get small bending radii, i.e. small device dimensions, we choose the best ridge possible to us with h = 2.1μm.

In Figure 5.2a shows the FEM calculated modal simulation for a 3 μm wide and 2.1 μm high guide with the two profiles reported in Figure 5.1. Figure 5.2b displays the fundamental mode at λ = 1500 nm of the same guide with the two profiles rescaled according to Sellmeier dispersions.

Note that these waveguide dimensions (especially the width) were chosen to fabricate a mono-modal waveguide at λ = 1500 nm.

5.1.2 EIM validation

Before fixing the gap, g, and the bend radius R we have to validate the 3-D to 2-D transformation through the Effective index Method (see §2.1.1). To do so we

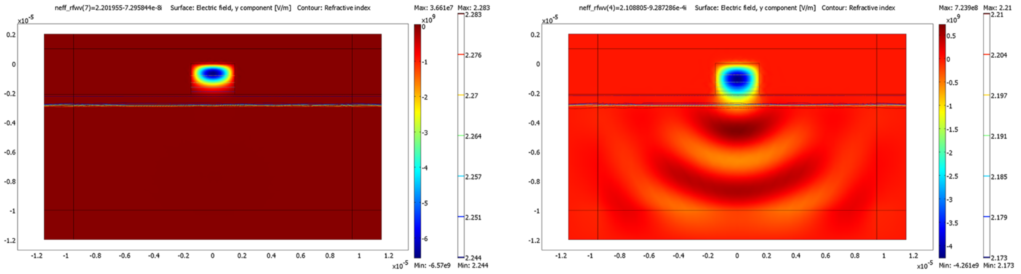

(a) (b)

Figure 5.2: *Fundamental mode FEM simulations at (a)* $\lambda = 632.8$ *nm and (b)* $\lambda = 1500$ *nm of a LiNbO*$_3$ *ridge waveguide with a width of 3 µm and a heighth of 2.1 µm. The refractive index profiles used are given in Figure 5.1.*

made a comparison between the effective index computed by the FEM simulations and the one given by the application of the EIM to our waveguide. The results are reported in Table 5.1.

	FEM	EIM		
λ (µm)	n_{eff}	n_s	n_f	n_{eff}
632.8	2.2019	1.0000	2.2043	2.2019
1400	2.1155	1.0000	2.1263	2.1153
1500	2.1088	1.0000	2.1210	2.1084
1600	2.1022	1.0000	2.1158	2.1016

Table 5.1: *EIM validation. Comparison between FEM and EIM for a waveguide with w* = 3 *µm at different working wavelengths.*

Note how the EIM approximation taken is good and lets us to assume air as surrounding medium. We can also consider LN as an isotropic material with a refractive index equal to the extraordinary one (i.e. TM polarised fundamental mode, see §4.1).

5.1.3 Bending loss

Now we can apply Eq (2.15) substituting the refractive indices computed by the EIM. The results are reported in Figure 5.3 according to the data given in Table 5.1. Note that a ring resonator with $R \geq 10$ µm has no bending loss.

We can proceed with the gap computation following the procedure illustrated in §2.1.3.

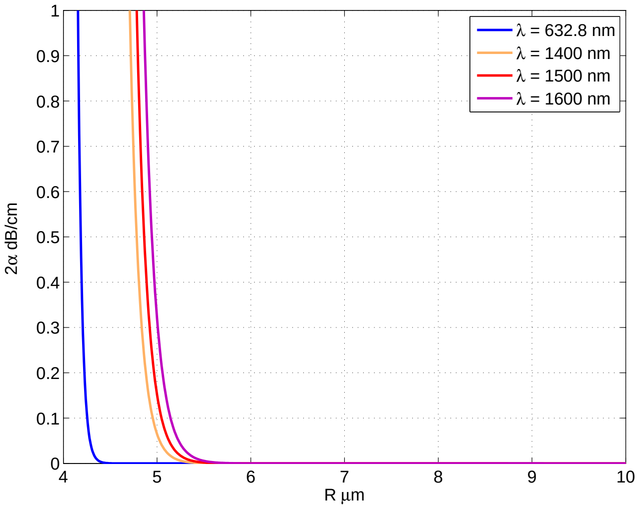

Figure 5.3: *Bending loss trends according to Table 5.1.*

5.1.4 Straight waveguides coupling

Before computing the coupling coefficient κ using Eq. (2.16), we need the expression of $\overline{E}_{t1}$ and $\overline{E}_{t2}$. They are both given by the resolution of a symmetric plane slab [5]. More in details we get (TM polarisation):

$$\begin{aligned} \overline{E}_{t1} \cdot \hat{y} &= E_{y1}(x) = -\eta_0 \frac{k}{\upsilon}\, b_2 e^{\upsilon x} \\ \overline{E}_{t2} \cdot \hat{y} &= E_{y2}(x) = \eta_0 \frac{k}{k_t}\, a_1 \cos\left(k_t\left(x + 2\,d + g\right)\right) \end{aligned} \tag{5.1}$$

where $d = w/2$ and

$$\begin{aligned} \upsilon &= \sqrt{n_{eff}^2\, k^2 - k^2\, n_s^2} \\ k_t &= \sqrt{k^2\, n_f^2 - n_{eff}^2\, k^2}. \end{aligned}$$

The expression of the power constants a_1 and b_2 are given in [5]. So Eq. (2.16) becomes:

$$\begin{aligned} \kappa &= \int_{-g-3\,d}^{-d-g} \frac{\omega}{4}\, \varepsilon_0 \left(n_f^2 - n_s^2\right) E_{y2}(x)\, E_{y1}(x)\, dx = \\ &= \frac{\omega\, \varepsilon_0 \left(n_c^2 - n_f^2\right) k^2\, \eta_0^2\, a_1\, b_2 e^{-\upsilon\,(2\,d+g)} \left(\upsilon \cos(k_t\, d) \sinh(\upsilon\, d) + k_t \sin(k_t\, d) \cosh(\upsilon\, d)\right)}{4\, k_t\, \upsilon \left(\upsilon^2 + k_t^2\right)}. \end{aligned} \tag{5.2}$$

Then we choose a value for η and applying Eq. (2.18) we get the plots reported in Figure 5.4 ($\eta^2 = 10^{-5}$).

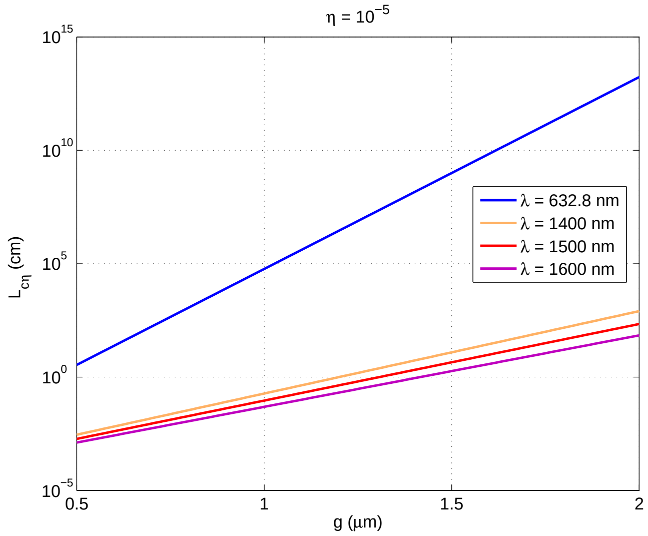

Figure 5.4: *Coupling length between two equal waveguides for $\eta^2 = 10^{-5}$ in function of the gap and the working wavelength.*

Since the smaller the gap is, the shorter the cavity length is and so the better FSR we get, we choose $g = 1$ µm.

5.1.5 Ring coupling

Now we will try to reach the critical coupling condition (see §2.1.3). Since we want to design on the worst case let's suppose that the inner circulating factor α_r is:

$$\alpha_r = e^{-\alpha_t L_{cav}}$$

where α_t represents all the loss mechanisms (e.g. by roughness, photolithographic imperfections, material absorption) that could not be taken into account by simulations. Only fabricating the device is possible to evaluate them.

So, recalling Eq. (2.18), we obtain for $g = 1$ µm the plot of τ and α_r in function of η^2 displayed in Figure 5.5.

Looking to these trends we decided to take $\eta^2 = 10^{-5}$ which means $L_{c\eta} = 918$ μm. The geometrical parameters of our device are summarised in Table 5.2.

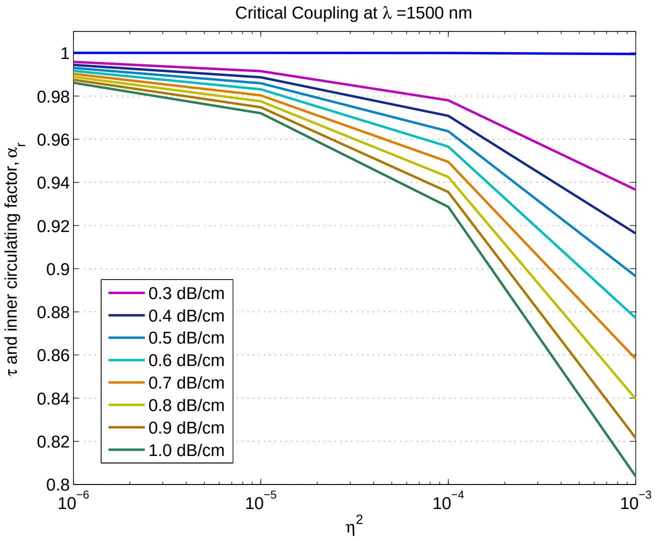

Figure 5.5: *Critical coupling at* $\lambda = 1500$ *nm with* $g = 1$ *µm.*

Parameter description	Parameter name	Value
Waveguides width	w	3.0 µm
Waveguides height	h	2.1 µm
Gap between the ring and the bus-bars	g	1.0 µm
Coupling length	$L_{c\eta}$	0.918 mm
Ring radius	R	100.0 µm

Table 5.2: *Geometrical parameters of the designed ring resonator.*

5.1.6 Fundamental parameters computation

Table 5.3 reports the values of Q (obtained from Eq. (2.23)), $\Delta\lambda_{3dB}$ (obtained from Eq. (2.21)) and $\mathcal{F}$ (obtained from Eq. (2.22)). The Free Spectral Range value is computed via Eq. (2.20) which yelds:

$$\Delta\lambda = 433 \text{ pm}.$$

So these are the theoretical performance of our $LiNbO_3$ ring resonator. Now we will proceed explaining the other research stream followed during this work: the refractive index tailoring.

5.2 Tailoring

Together with the device design and fabrication we decide to put more attention to the refractive index distributions. So we performed a series of refractive

α_t (db/cm)	Q	$\Delta\lambda_{3dB}$ (pm)	$\mathfrak{F}$
0.3	6.39E+05	2.35	185
0.4	4.80E+05	3.13	138
0.5	3.84E+05	3.91	111
0.6	3.20E+05	4.69	92
0.7	2.74E+05	5.47	79
0.8	2.40E+05	6.25	69
0.9	2.13E+05	7.03	62
1.0	1.92E+05	7.82	55

Table 5.3: *Ring resonator fundamental parameters computation. The worst case is highlighted in yellow*

index measurements at different wavelengths [52] on different samples implanted with 3.9 MeV C ions at a fluence of 4×10^{14} ions/cm^2. These measurements are illustrated in the next section.

5.2.1 M-lines

The technique employed to measure both the refractive indices of our LN sample is called dark m-lines [56] and is based on a prism coupler. In brief, this method works as follows.

The coupling of a laser beam by a prism into a planar dielectric waveguide is governed by the angle θ of incidence of the light onto the prism base (Figure 5.6). This angle determines the phase velocity in y direction, $\beta = c/n_p \sin\theta$, of the incident wave in the prism (index n_p) and in the gap.

Strong coupling of light into the film occurs only when we choose θ so that β equals the phase velocity β_m of one of the characteristic modes of propagation in the guide ($m = 0, 1, 2, \ldots$).

So using the relation reported in [56] is possible to compute the effective indices of the propagating modes. A view of the measurements setup is given in Figure 5.7a.

The sample is mounted on a high precision rotary stage and the output intensity is measured with a large area silicon PIN photodiode (Figure 5.7b). The resolution in n_{eff} evaluations is estimated better than 0.001, mainly determined by the uncertainty on apex angle and refractive indices of rutile prism and by the precision of angle measurements.

The waveguide properties of two samples (z-cut wafer as implanted, AI, and annealed, ANN, for 2 hours at 280 °C) have been investigated using this setup.

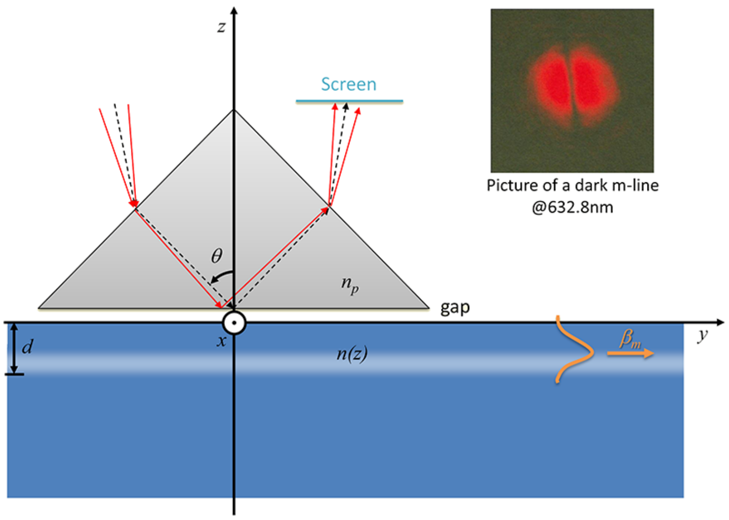

Figure 5.6: *Schematic cross section through a prism-film coupler applied to our case.*

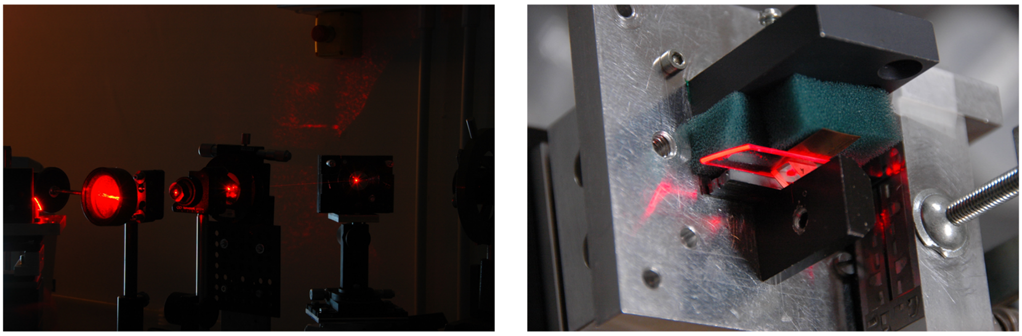
(a) (b)

Figure 5.7: *Dark m-lines measurement setup. (a) Beam line with a mirror, two polarisers and a focus lense. (b) Detail of the light spot visible between the prism and the sample.*

Both TE (for n_o) and TM (for n_e) modes effective indices (n_{eff}) of the samples were measured at three different wavelengths: $\lambda = 532, 632.8, 818$ nm.

Figures 5.8a and 5.8b show respectively the measured n_{eff} of TE and TM modes in the AI and ANN samples. The Sellmeier dispersion curves [40] of the substrate are also shown as reference.

Effective indexes of TE and TM "mode 0" (higher measured n_{eff} values) are close to the n_o and n_e Sellmeier curves respectively. They systematically lie below the substrate values in the case of n_o and above the substrate values in the case of n_e. This is a well known characteristic of ion implanted LN waveguides generi-

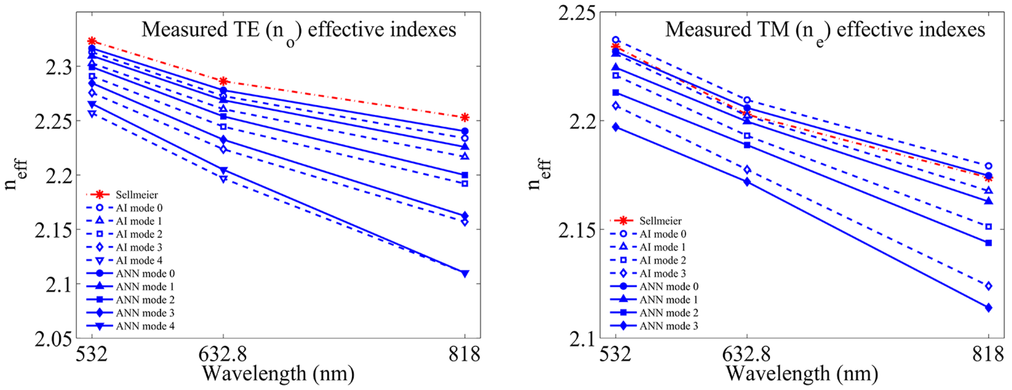

(a) (b)

Figure 5.8: *Dark m-lines measurement results for (a) TE and (b) TM modes.*

cally attributed to a reduction of birefringence (decrease of n_o, increase of n_e) due to ion damage in the surface region [45].

The annealing process acts in opposite directions on n_o and n_e, moving the TE modes towards higher n_{eff} values and TM modes towards lower n_{eff} values. This reflects an overall increasing of n_o and a lowering of n_e mean value that can be partially ascribed to birefringence recovery due to the annealing process [52].

These measurements allows us to correct the curves of Figure 3.5 with those reported in Figure 5.9.

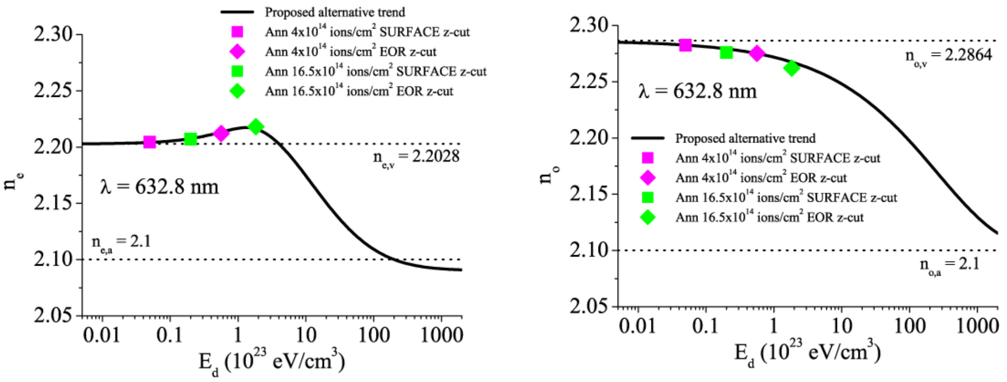

(a) (b)

Figure 5.9: *Refractive index tailoring in Lithium Niobate by ion implantation. Best fit curves of literature data of (a) n_e and (b) n_o distributions in function of E_d [52] corrected with the measurements reported in Figure 5.8.*

Appling these two distributions to the case of 3.9 MeV C ions at a fluence of

4×10^{14} ions/cm^2 followed by annealing, we obtain the two profiles reported in Figure 5.10.

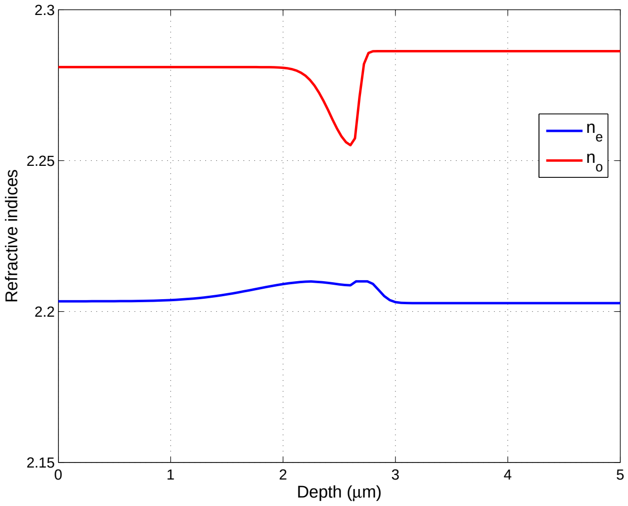

Figure 5.10: *Refractive index profiles of n_e and n_o at $\lambda = 632.8$ nm according with [52] for LiNbO$_3$ ion-implanted with 3.9 MeV C ions at a fluence of 4×10^{14} ions/cm^2 followed by annealing.*

These profiles were also calculated using the Reflectivity Calculation Method (RCM) [57], applied to the m-lines measurements at $\lambda = 632.8$ nm, assuming a two half-Gaussian structure for n_o and a more complex one for n_e taking into account the buried raised-index region [52].

Note how these new profiles are different from those reported in Figure 5.1. Besides the fact that the ordinary profiles are quite similar, the extraordinary ones have substantially opposite trends. This fact yields to an E_y distribution for the fundamental TM mode of the type reported in 5.11. The waveguide dimensions are the same of Figure 5.2.

From Figure 5.11b we notice that, at $\lambda = 1500$ nm this waveguide doesn't work. However this waveguide is still a waveguide for visible light.

5.3 Fabrication issues

In this section we will focus our attention on the main issues faced during the fabrication of our prototypes. This technological issues have changed the original behaviour of the resonators. However their impact is less critical compared to what we have presented above regarding the refractive index profiles.

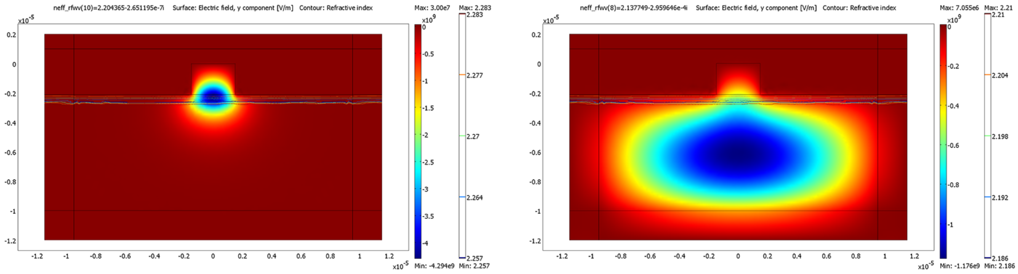

(a) (b)

Figure 5.11: *Fundamental mode FEM simulations at (a)* $\lambda = 632.8$ *nm and (b)* $\lambda = 1500$ *nm of a LiNbO*$_3$ *ridge waveguide with a width of 3 µm and a heighth of 2.1 µm. The refractive index profiles used are given in Figure 5.10.*

5.3.1 Temperature

Let's start from a basilar problem: thermal treatment of Lithium Niobate. Its pyroelectricity, i.e. the change in spontaneous polarisation as a function of temperature, is due to the movement of the lithium and niobium ions relative to the oxygen layers [1]. Since the Li and Nb ions move only in a direction parallel to the c-axis, z, in the case of z-cut wafer this effect is maximum (see Chapter 3).

The initial annealing made to recover the point-defects produced by ion implantation (see §3.2) is, in fact, performed with two ramp with a precise timing (less than 10 °C/min for heating and less than 4 °C/min for cooling) to avoid thermal stress that could break the crystal through sparks.

Even if we followed these precautions during all the procedure (i.e. for each bake that the conventional photolithography requires) a wafer broke making us restart the run with another one.

5.3.2 Photoresist

The photoresist used as masking layer for our ridge waveguides, as pointed out in §4.2, is commonly used at CNR-IMM Laboratories of Bologna for the metal layer definition through "liftoff" processes.

In other words, the metal sputtering/evaporating step is performed *after* the photolithographic patterning of the PR and consequently the removal of the resist lift the metal off defining electrodes in an opposite way respect the one we used for our electrodes definition (i.e. the mask tone is the opposite, see §4.3.3).

An example of the photoresist cross section is given by Figure 5.12. Looking at this shape makes clear its application, in fact, the aspect ratio is made to respect the feature size at the surface and to minimise the contact with the layer below.

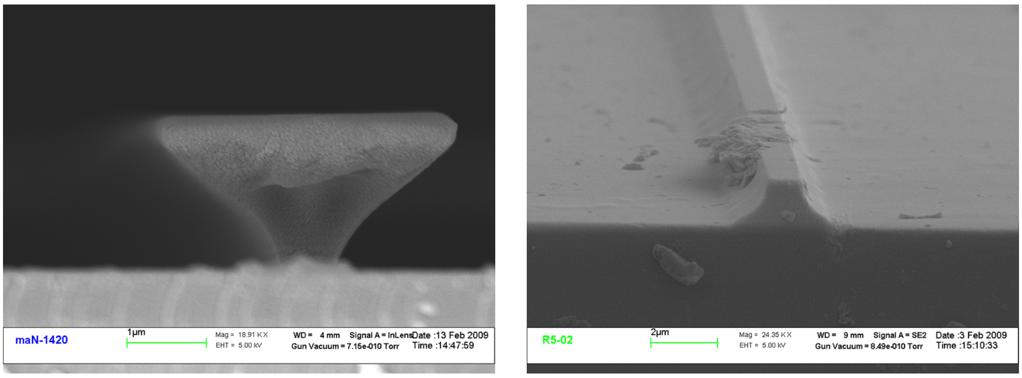

(a) (b)

Figure 5.12: *Negative PR cross section. (a) Patterned photoresist. (b) SEM image of the ridge waveguide obtained.*

Figure 5.12b, together with Figures 4.6b and 4.9b, demonstrate how ion-implantation transfers well the masking layer to the crystal, as pointed out in §3.2.2. So, the fundamental mode of the real waveguide is reported in Figure 5.13, with the index profiles of Figure 5.10.

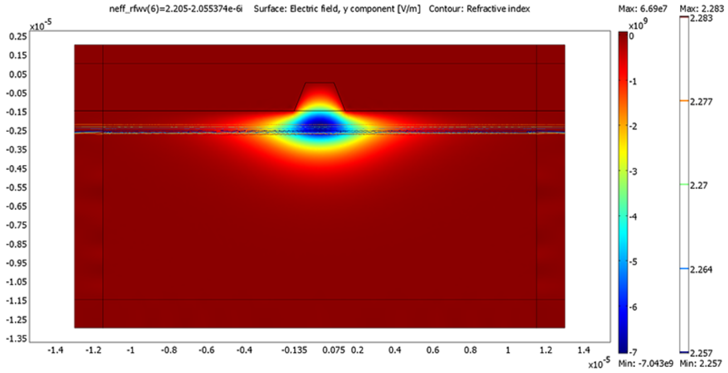

Figure 5.13: *Fundamental mode FEM simulation at* $\lambda = 632.8$ *nm of the* $LiNbO_3$ *ridge waveguide fabricated. The refractive index profiles used are given in Figure 5.10. The cross section is the one reported in Figure 4.6b.*

Another pattern transferring issue caused by this particular photoresist is shown in Figure 5.14. As pointed before (§4.3.3), only 2 of the 80 devices were fabricated with the gap between the busbars and the ring.

The last problem connected to the PR is the fact that it cannot effort more than two implantation/etching steps since it is completely carbonised by ion-implantation and is very difficult to remove it with the conventional technique

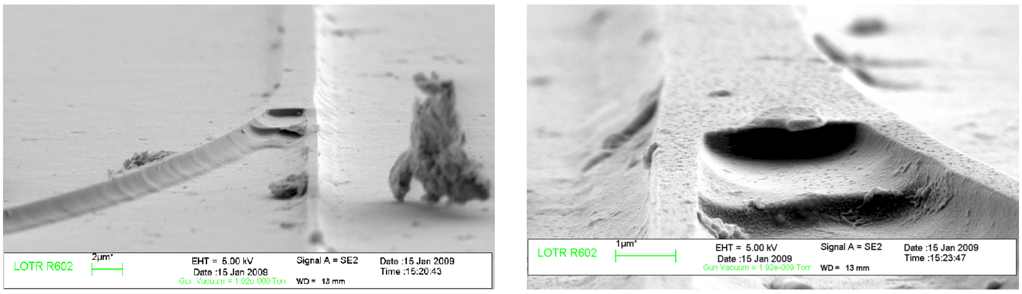

Figure 5.14: *SEM images of the coupling region between the straight waveguide and the ring resonator. Note the pattern doubling in proximity of the junction, due to double implantation/etching step, and the absence of the gap.*

(§4.3.2).

For this reason at the end of the whole procedure our ridges have an height of 1.4 µm instead of 2.1 µm (i.e. three implantation/etching steps) as initially thought.

5.3.3 Metal adhesion and jump sparks

The last two technological issues encountered are connected to the Aluminium layer and the electrodes definition step (see §4.3.3).

The first one is illustrated by an example shown in Figure 5.15: in some devices (~ 20%) in the region were the Al layer crosses the ridge waveguide the film is lifted up an consequently the oxide layer below was attacked by the RIE process.

This problem is caused both by the track width designed (too narrow) and also by a definition process adopted for the first time. In fact, as pointed out before, the metal film definition technique usually performed at IMM of Bologna, is liftoff based (see §5.3.2).

Moreover, the charge accumulated by the $LiNbO_3$ during the RIE process as a consequence of its ferroelectricity caused jump sparks between near tracks and consequently the breaking of them (~ 10% of the devices affected by this problem). Figure 5.16 shows this phenomenon that occurs despite the rounded design of the tracks.

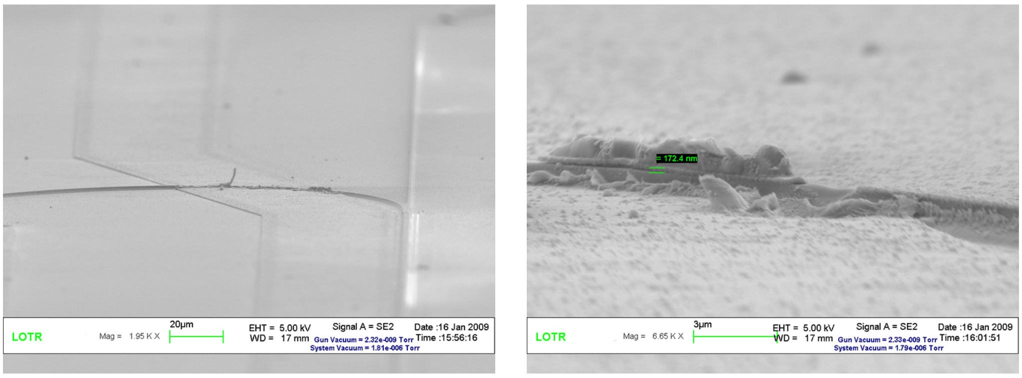

(a) (b)

Figure 5.15: *SEM images of the cross region between an electrode track and the microring. (a) General view with Al lifted up. (b) Detail of the crossing with silicon dioxide etched.*

Figure 5.16: *Optical images of the tracks broken by point effect.*

5.4 Optical characterisation

All the results illustrated in the past sections put all together let us both to verify the refractive index profile trends, that were not known at the time, and to proceed with a new design phase with well established basis.

Before illustrating our new device proposal we need to confirm the simulation illustrated in Figure 5.13. Since we know that the fabricated waveguides work at $\lambda = 632.8$ nm we decide to perform some near field measurements at this wavelength.

5.4.1 Near Field Measurements

We built the setup for *Near Field* measurements [58] shown in Figure 5.17a. This technique allows to measure the intensity of a beam of light coming out from the waveguide.

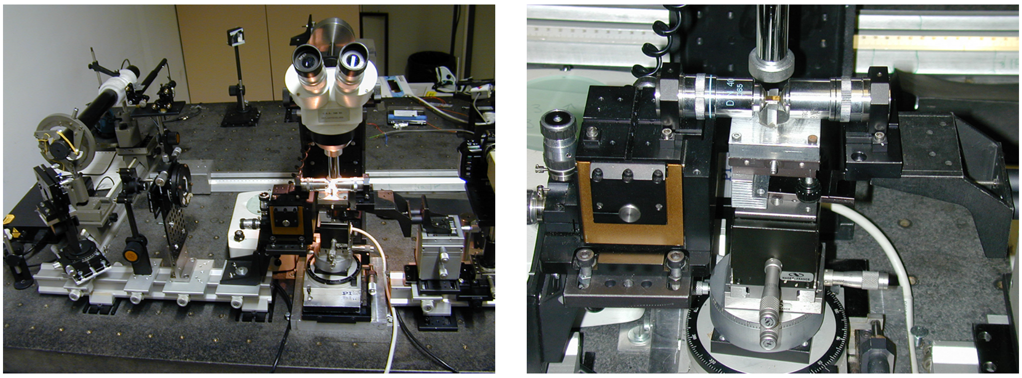

(a) (b)

Figure 5.17: *Built setup for Near field measurements. (a) View of the beam line, the nanometric input stage, the sample-holder and the micrometric output stages. (b) Detail of the two objective butt coupled with the sample beneath a stereoscope.*

The setup works as follows. A laser beam is focused by an objective (magnifying factor, $M = 40$) at the input surface of the sample which was optically prepared to avoid scattering (see §4.3.4) . Then the output light is collected by another objective ($M = 60$) at a distance of 15 cm from it (i.e. the objective Back Focal Length, BFL) the CCD detector is placed.

Before measuring the near field intensity one microring resonator we tested the setup on an embedded waveguide produced through ion implantation. This waveguide was obtained masking an x-cut LN wafer with an Au layer thick 1.1 μm before performing an ion-implantation with 3.9 MeV C ions at a fluence of 4×10^{14} ions/cm^2 followed by annealing (Figure 5.18a).

The simulated main electric component of the fundamental mode for extraordinary polarisation (TE in this case so E_x) is reported in Figure 5.18b.

Figure 5.19a shows the near field image of the fundamental mode of an embedded waveguide with $w = 9.5$ μm. The total power distribution computed by COMSOL is reported in Figure 5.19b.

The comparisons between simulation and measurement, with a very good agreement, are reported in Figure 5.19c (horizontal section) and 5.19d (vertical section).

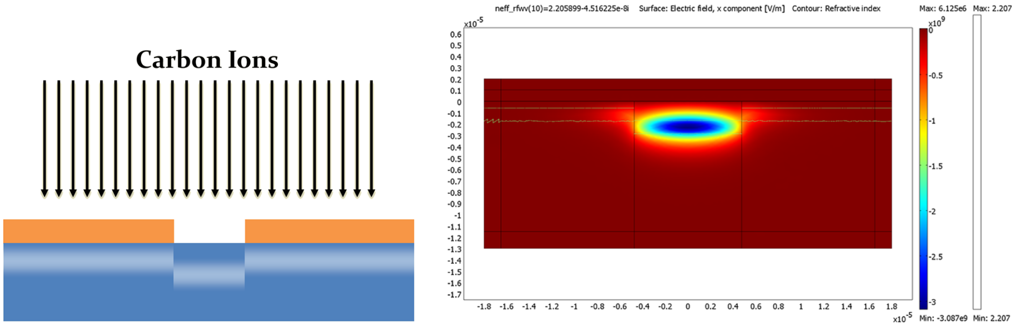

(a) (b)

Figure 5.18: *Embedded ion-implanted waveguide. (a) Fabrication concept. (b) Fundamental mode FEM simulation at* $\lambda = 632.8$ *nm of an embedded waveguide 9.5 µm wide. The refractive index profiles used are given in Figure 5.10.*

Finally Figure 5.20a shows the near field measurement of one of our devices. The simulated power distribution for the same device is given in 5.20b.

In this case there is not the good agreement between the measured data and the simulation as in the embedded waveguide. In fact, in Figure 5.20a we recognise also the superimposition of the fundamental mode of the plane slab obtained by the C ions implantation.

Recall Figure 4.1a, the four device ports were spaced of 2 mm to permit fibre coupling and to do so each bus-bar was designed with bent waveguides with R in according with Table 5.2.

However reapplying the procedure shown in §5.1 one obtains $R > 2$ mm for negligible bending loss. That means that a bend radius of 100 µm for the waveguide fabricated (recall Figure 5.13) is too narrow and send out of propagation the light injected into the waveguide.

Now that all the issues encountered are explained we can conclude this chapter illustrating a different waveguide which resolves many of these problems and can be used as starting point for the design of new microring resonators.

5.5 New device proposal

In this section the possibility to fabricate efficient waveguides in the telecommunication band using ion-implantation technology will be illustrated showing how powerful this method is.

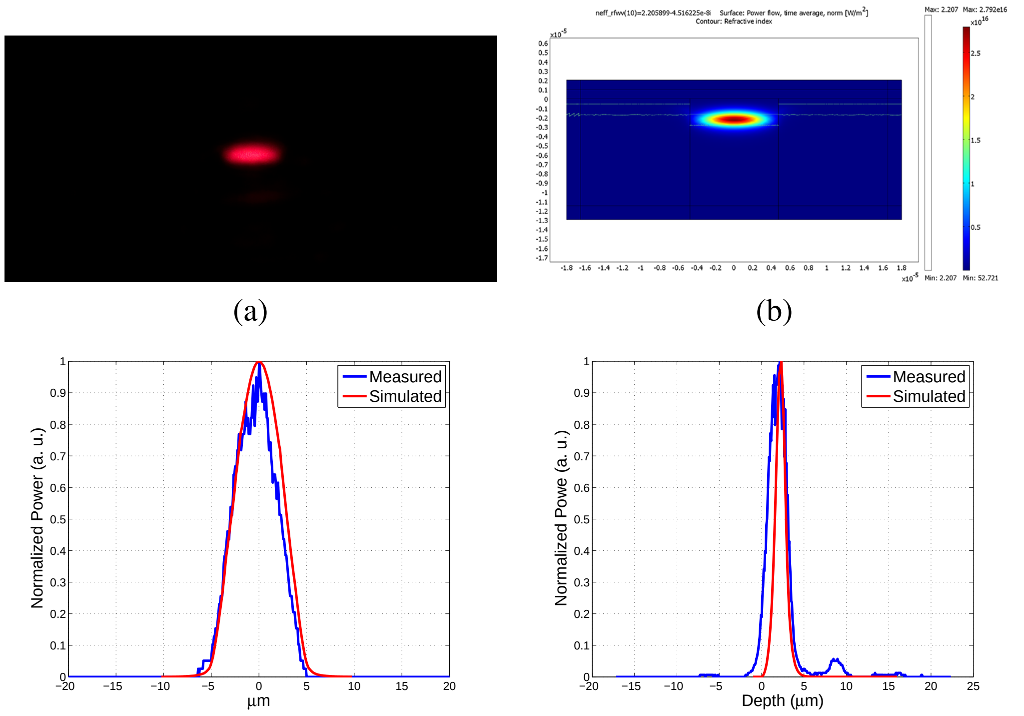

(a) (b)

(c) (d)

Figure 5.19: *Near Field measure of an embedded waveguide at $\lambda = 632.8$ nm. (a) CCD data. (b) Simulated power distribution for the fundamental mode. Comparison between the measured data and the simulation for (c) an horizontal section and (d) a vertical one.*

5.5.1 Alternative implantation recipe

First of all the refractive index profiles shown in Figure 5.10 can be substituted by two different ones with stronger variation that means a better light confinement.

So using our refractive index model (see §3.2.1) we implanted a z-cut LN sample with 3.9 MeV C ions at a fluence of 16.5×10^{14} ions/cm^2 followed by annealing (2 h at 280 °C).

Then we measured it with the dark m-lines technique at $\lambda = 632.8$ and, using the RCM algorithm (see §5.2.1), we obtained the two profiles shown in Figure 5.21. These two profiles are in very good agreement with our tailoring model.

5.5.2 Alternative photoresist

A lot of problems occur with the particular photoresist employed. So a better alternative is SU-8: an high aspect ratio negative PR well known in Electronics

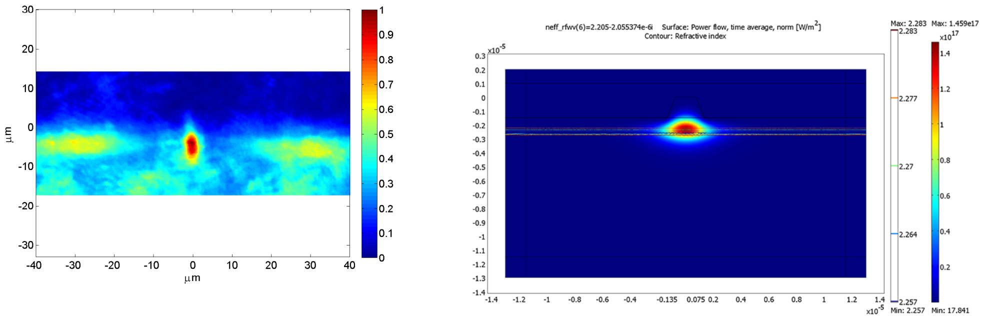

(a) (b)

Figure 5.20: *Near Field measure of ridge waveguide at* λ = 632.8 *nm. (a) Measured intensity distribution. (b) Simulated power distribution for the fundamental mode.*

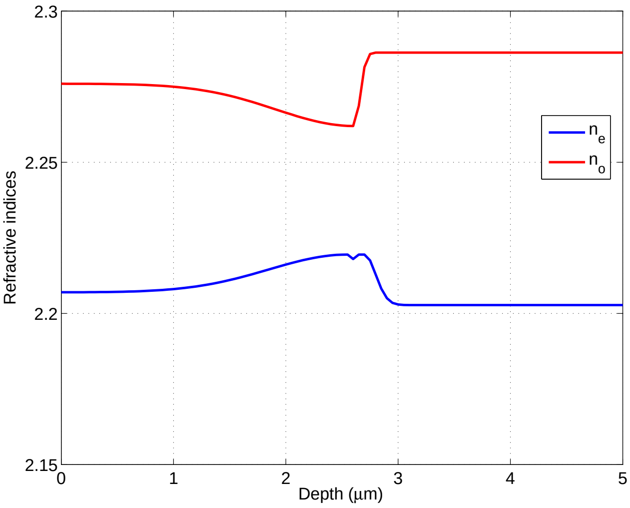

Figure 5.21: *Refractive index profiles of* n_e *and* n_o *at* λ = 632.8 *nm according with [52] for* $LiNbO_3$ *ion-implanted with 3.9 MeV C ions at a fluence of* 16.5×10^{14} *ions/cm*^{2} *followed by annealing.*

and Optics [55]. Figure 5.22 shows SU-8 patterned with our devices mask with excellent results.

Since SU-8 has higher aspect ratio than ma-N 1420, it allows us to amorphise more than 2 μm in a single step so we can fabricate, with two implantation /etching steps a ridge high at least 4 μm.

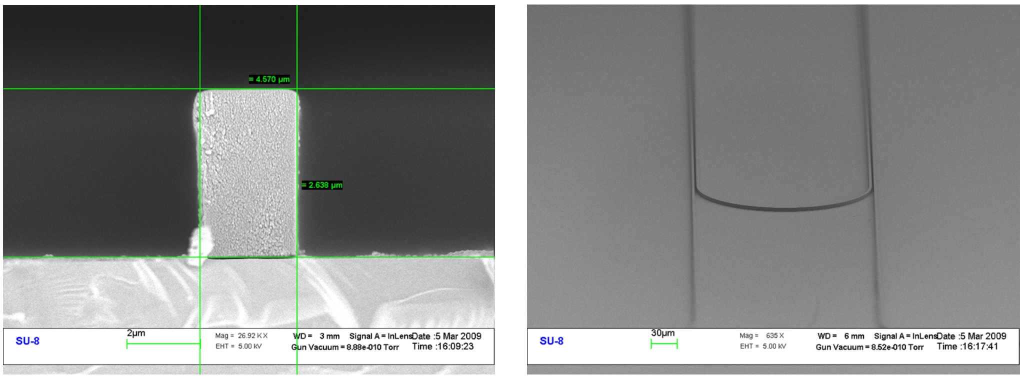

(a) (b)

Figure 5.22: *SU-8 PR patterned with our devices photomask. (a) Cross section. (b) Ring resonator footprint with gaps definition.*

5.5.3 Final result

Combining the new refractive index profiles, the SU-8 photoresist and the possibility to etch 4 µm of $\mathrm{LiNbO_3}$ the new ridge waveguide is displayed in Figure 5.23. Its dimensions are: w = 6 µm and h = 4 µm.

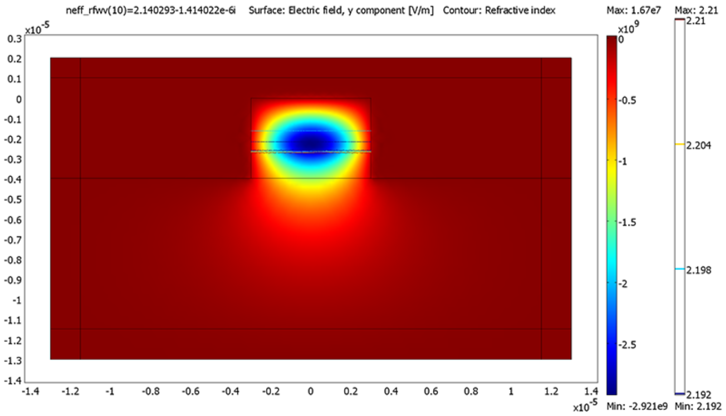

Figure 5.23: *Fundamental mode FEM simulation at* λ = 1500 *nm of the* $\mathrm{LiNbO_3}$ *new ridge waveguide. The refractive index profiles are those given in Figure 5.21 rescaled with Sellmeier equations.*

Note that the simulation is performed at λ = 1500 nm. In conclusion we obtained a mono-modal ridge waveguide in the telecom band with a rectangular section as we desired at the beginning of this work.

Conclusions and Future Work

This thesis described the work I have done in the last three years at the CNR-IMM (Istituto per la Microelettronica e i Microsistemi) of Bologna studying and realising optical microresonator in Lithium Niobate for telecom and sensing applications. The main challenge was the realisation of these devices with a technology which was routinely used at CNR-IMM for Silicon substrates, but not yet for this material

For the first time optical ring resonators were fabricated in Lithium Niobate using only ion-implantation based technology to confine light inside the structures.

A complete device fabrication process was then setup and performed starting from the theoretical modelling, the CAD design, the technological realisation up to the final characterisation.

Ion-implantation is a powerful tool for refractive index profiles tailoring of LN. For the first time on an international scale a method of refractive index profiles engineering was proposed. This method gives the possibility to design optical waveguides tuned on different working frequencies depending on the desired application.

For the first time on an international scale, a method of etching rate engineering through ion-implantation was developed. This method lets us to fabricate ridge waveguides and other tridimensional structures. The results are very encouraging: even preliminary samples show that the developed technological process allows the fabrication of waveguides with very low sidewall roughness.

The combination of this two methods and the solutions of some issues concerning the adaptation of silicon planar technologies to a very different substrate, lets us to develop a new technological process. This procedure allows us to fabricate complex integrated optical devices in Lithium Niobate.

Moreover a complete set of analytical and numerical tools were developed to design ring resonators using this particular technology taking into account all its peculiarities and challenges.

Even the measurement setup were designed and built to perform the necessary characterisation of such devices and the future ones.

Now, thanks to the experience matured during this training period, we are ready to fabricate a new set of devices. The first steps into a new research path has just been taken.

Publications

- G.G. Bentini, M. Chiarini,M. Bianconi, F. Bergamini, D. Castaldini, **G.B. Montanari**, A. Bogoni, L. Potì, S. Sugliani, A. Nubile, P. De Nicola, L. Gallerani, G. Pennestrì, S. Petrini, "Waveguide formation by ion implantation in Er doped optical materials," *Nuclear Instruments & Methods in Physics Research B*, vol. 266, pp. 3120-3124, 2008.
- M. Bianconi, G.G. Bentini, M. Chiarini, P. De Nicola, **G.B. Montanari**, A. Nubile, S. Sugliani, "Defect engineering and micromachining of Lithium Niobate by ion implantation," *Nuclear Instruments & Methods in Physics Research B* vol. 267, pp. 2839-2845, 2009.
- S. Sugliani, M. Bianconi, G. G. Bentini, M. Chiarini, P. De Nicola, **G.B. Montanari**, A. Menin, A. Malacarne, L. Potì, "Refractive index tailoring in Lithium Niobate by ion implantation," submitted to *Nuclear Instruments & Methods in Physics Research B*.

Bibliography

[1] K. K. Wong, ed., *Properties of Lithium Niobate*, no. 28 in EMIS Datareviews, (London, United Kingdom), INSPEC, The Institution of Electrical Engineers, 2002.

[2] D. Castaldini, *Study, fabrication and charaterization of Segmented Waveguides for advanced photonic components on Lithium Niobate*. PhD thesis, University of Bologna, Italy, 2006.

[3] P. Bassi, L. Scolari, and R. Zoli, *Propagazione di Onde Elettromagnetiche*. Clueb, 2006.

[4] V. Rizzoli and A. Lipparini, *Propagazione Elettromagnetica Guidata*. Esculapio Progetto Leonardo, 2002.

[5] P. Bassi, G. Bellanca, and G. Tartarini, *Propagazione ottica libera e guidata*. Clueb, 1999.

[6] S. C. Hagness, *FDTD Computational Electromagnetics Modeling of Microcavity Lasers and Resonant Optical Structures*. PhD thesis, University of Evanston, Illinois, USA, June 1998.

[7] J. L. Jewell, J. P. Harbision, A. Scherer, Y. H. Lee, and L. Florez, "Vertical-cavity surface-emitting lasers - design, growth, fabrication, characterization," *IEEE Journal of Quantum Electronics*, vol. 27, pp. 1332–1346, June 1991.

[8] J. D. Joannopoulos, P. R. Villeneuve, and S. H. Fan, "Photonic crystals: Putting a new twist on light," *Nature*, vol. 386, pp. 143–149, March 1997.

[9] M. Gnan, G. Bellanca, H. M. H. Chong, P. Bassi, and R. M. D. L. Rue, "Modelling of photonic wire bragg gratings," *Optical and Quantum Electronics*, vol. 38, pp. 133–148, 2006.

[10] M. Cai, O. Painter, K. J. Vahala, and P. C. Sercel, "Fiber-coupled microsphere laser," *Optics Letters*, vol. 25, pp. 1430–1432, October 2000.

[11] M. L. Gorodetsky, A. A. Savchenkov, and V. S. Ilchenko, “Ultimate Q of optical microsphere resonators,” *Optics Letters*, vol. 21, pp. 453–455, April 1996.

[12] I. Teraoka and S. Arnold, “Whispering-gallery modes in a microsphere coated with a high-refractive index layer: polarization-dependent sensitivity enhancement of the resonance-shift and TE-TM resonance matching,” *Journal of the Optical Society of America B - Optical Physics*, vol. 24, pp. 653–659, March 2007.

[13] M. Cai, O. Painter, and K. J. Vahala, “Observation of critical coupling in a fiber taper to a silica-microsphere whispering-gallery mode system,” *Physical Review Letters*, vol. 85, pp. 74–77, July 2000.

[14] M. L. Gorodetsky and V. S. Ilchenko, “Optical microsphere resonators: optimal coupling to high-Q whispering-gallery modes,” *Journal of the Optical Society of America B - Optical Physics*, vol. 16, pp. 147–154, January 1999.

[15] S. Berneschi, *Microlaser in Rare Earths Doped Glasses*. PhD thesis, University of Bologna, Italy, 2007.

[16] B. E. Little, S. T. Chu, H. A. Haus, J. Foresi, and J.-P. Laine, “Microring resonator channel dropping filters,” *Journal of Lightwave Technology*, vol. 15, no. 6, pp. 998–1005, 1997.

[17] B. E. Little, J. S. Foresi, G. Steinmeyer, E. R. Thoen, S. T. Chu, H. A. Haus, E. P. Ippen, L. C. Kimerling, and W. Greene, “Ultra-compact Si-SiO2 microring resonator optical channel dropping filters,” *IEEE Photonics Technology Letters*, vol. 10, pp. 549–551, April 1998.

[18] J. Niehusmann, A. Vrckel, and P. H. Bolivar, “Ultrahigh-quality-factor silicon-on-insulator microring resonator,” *Optics Letters*, vol. 29, pp. 2861–2863, 2004.

[19] C.-Y. Chao, W. Fung, and L. J. Guo, “Polymer microring resonators for biochemical sensing applications,” *Journal of Selected Topics in Quantum Electronics*, vol. 12, pp. 134–142, 2006.

[20] P. Koonath, T. Indukuri, and B. Jalalib, “Add-drop filters utilizing vertically coupled microdisk resonators in silicon,” *Applied Physics Letters*, vol. 86, no. 091102, 2005.

[21] F. Michelotti, A. Driessen, and M. Bertolotti, eds., *Microresonators as building blocks for VLSI photonics*, vol. 709, AIP Conference, American Istitute of Physics, Melville, New York, 2004.

[22] M. Hammer, K. R. Hiremath, and R. Stoffer, “Analytical approaches to the description of optical microresonator devices,” *Microresonators as building blocks for VLSI photonics: International School of Quantum Electronics, 39th Course*, vol. 709, no. 1, pp. 48–71, 2004.

[23] G. Cusmai, F. Morichetti, P. Rosotti, R. Costa, and A. Melloni, “Circuit oriented modelling of ring-resonators,” *Optical and Quantum Electronics*, vol. 37, pp. 343–358, January 2005.

[24] L. Prkna, J. Čtyroký, and M. Hubálek, “Ring microresonator as a photonic structure with complex eigenfrequency,” *Optical and Quantum Electronics*, vol. 36, pp. 259–269, 2004.

[25] K. R. Hiremath, *Coupled Mode Theory Based Modeling and Analysis of Circular Optical Microresonators*. PhD thesis, University of Twente, Nederlands, 2005.

[26] D. J. W. Klunder, E. Krioukov, F. S. Tan, T. V. der Veen, H. F. Bulthuis, G. Sengo, C. Otto, H. J. W. M. Hoekstra, and A. Driessen, “Vertically and laterally waveguide-coupled cylindrical microresonators in Si_3N_4 on SiO_2 technology,” *Applied Physics B*, vol. 73, pp. 603–608, 2001.

[27] M. K. Chin and S. T. Ho, “Design and modeling of waveguide-coupled single-mode microring resonators,” *Journal of Lightwave Technology*, vol. 16, pp. 1433–1446, 1998.

[28] P. Cheben, R. Soref, D. Lockwood, and G. Reed, eds., *Silicon Photonics*, Hindawi Publishing Corporation, 2008.

[29] P. Dumon, W. Bogaerts, V. Wiaux, J. Wouters, S. Beckx, J. V. Campenhout, D. Taillaert, B. Luyssaert, P. Bienstman, D. V. Thourhout, and R. Baets, “Low-loss soi photonic wires and ring resonators fabricated with deep uv lithography,” *IEEE Photonics Technology Letters*, vol. 16, no. 5, pp. 1328–1330, 2004.

[30] H. J. M. Bastiaansen, *Modal Analysis of Straight and Curved Integrated Optical Waveguides, An integral equation approch*. PhD thesis, Delft University, The Netherlands, 1994.

[31] L. Rayleigh, “The problem of the whispering gallery,” *Scientific Papers, Cambridge University*, vol. 5, pp. 617–620, 1912.

[32] M. Abramowitz and I. A. Stegun, *Handbook of Mathematical Functions with Formulas, Graphs, and Mathematical Tables*. New York: Dover, 9^{th} dover printing, 10^{th} GPO printing ed., 1964.

[33] D. Marcuse, *Light transmission optics*. New York, USA: Van Nostrand Reinhold Company, 2^{nd} ed., 1982.

[34] A. Yariv, "Universal relations for coupling of optical power between microresonators and dielectric waveguides," *Electronics Letters*, vol. 36, pp. 321–322, May 2000.

[35] T. Itho, ed., *Numerical Techniques for Microwave and Millimeter-Wave Passive Structures*, Wiley, 1989.

[36] G. Bellanca, *Un simulatore elettromagnetico FDTD con applicazioni nel settore del riscaldamento a microonde*. PhD thesis, Università degli Studi di Bologna, Italy, 1994.

[37] A. Vorckel, M. Monster, W. Henschel, P. H. Bolivar, and H. Kurz, "Asymmetrically coupled silicon-on-insulator microring resonators for compact add-drop multiplexers," *Photonics Technology Letters, IEEE*, vol. 15, no. 7, pp. 921–923, 2003.

[38] G. B. Montanari, "Studio di risonatori ad anello ottici integrati tramite tecniche fdtd," Master's thesis, Università degli Studi di Bologna, Italy, 2005.

[39] T.-J. Wang, C.-H. Chu, and C.-Y. Lin, "Electro-optically tunable microring resonators on lithium niobate," *Optics Letters*, vol. 32, no. 19, pp. 2777–2779, 2007.

[40] Crystal Technology, Inc., "Lithium Niobate optical crystals." Data sheet.

[41] D. A. Cohen, *Lithium Niobate microphotonic modualtors*. PhD thesis, University of Southern California, USA, 2001.

[42] C. Kittel, *Introduction to Solid State Physics*. Wiley, 8^{th} ed., 2005.

[43] M. Born and E. Wolf, *Principles of Optics: Electromagnetic Theory of Propagation, Interference and Diffraction of Light*. Cambridge University Press, 7^{th} ed., October 1999.

[44] G. G. Bentini and R. Galloni, *Impiantazione Ionica*. Clueb, 1975.

[45] F. Chen, "Photonic guiding structures in lithium niobate crystals produced by energetic ion beams," *Journal of Applied Physics*, vol. 106, no. 081101, pp. 1–29, 2009.

[46] M. Bianconi, F. Bergamini, S. Cristiani, and G. Lulli, "Ion implantation of silicon at the nanometer scale," *Journal of Applied Physics*, vol. 102, October 2007.

[47] M. Bianconi, N. Argiolas, M. Bazzan, G. G. Bentini, M. Chiarini, A. Cerutti, P. Mazzoldi, G. Pennestri, and C. Sada, "Nuclear and electronic energy loss synergy in the process of damage growth in ion implanted $LiNbO_3$," *Nuclear Instruments & Methods in Physics Research B*, vol. 249, pp. 122–125, August 2006.

[48] G. G. Bentini, M. Bianconi, L. Correra, M. Chiarini, P. Mazzoldi, C. Sada, N. Argiolas, M. Bazzan, and R. Guzzi, "Damage effects produced in the near-surface region of x-cut $linbo_3$ by low dose, high energy implantation of nitrogen, oxygen, and fluorine ions," *Journal of Applied Physics*, vol. 96, pp. 242–247, July 2004.

[49] J. F. Ziegler, J. P. Biersack, and U. Littmark, *The Stopping and Ranges of Ions in Solids*, vol. 1. New York, USA: Pergamon, 1985. SRIM web page: http://www.srim.org.

[50] M. Bianconi, G. G. Bentini, M. Chiarini, P. De Nicola, G. B. Montanari, A. Nubile, and S. Sugliani, "Defect engineering and micromachining of Lithium Niobate by ion implantation," *Nuclear Instruments & Methods in Physics Research B*, vol. 267, pp. 2839–2845, September 2009.

[51] M. Bianconi, G. G. Bentini, M. Chiarini, P. D. Nicola, G. Montanari, A. Menin, A. Nubile, and S. Sugliani, "Simulation of electronic damage induced by ion implantation in Lithium Niobate." submitted to Nuclear Instruments & Methods in Physics Research B, 2010.

[52] S. Sugliani, M. Bianconi, G. G. Bentini, M. Chiarini, P. D. Nicola, G. B. Montanari, A. Menin, A. Malacarne, and L. Pot, "Refractive index tailoring in lithium niobate by ion implantation." submitted to Nuclear Instruments & Methods in Physics Research B, 2010.

[53] J. Reinisch, F. Schrempel, T. Gischkat, and W. Wesch, "Etching of ion irradiated $LiNbO_3$ in aqueous hydrofluoric solutions," *Journal of the Eletrochemical Society*, vol. 155, no. 4, pp. D298–D301, 2008.

[54] M. Bianconi, F. Bergamini, G. G. Bentini, A. Cerutti, M. Chiarini, P. De Nicola, and G. Pennestri, "Modification of the etching properties of x-cut Lithium Niobate by ion implantation," *Nuclear Instruments & Methods in Physics Research B*, vol. 266, pp. 1238–1241, April 2008.

[55] C. C. Hu, *Modern Semiconductor Devices for Integrated Circuits*. Prentice Hall, March 2009.

[56] R. Ulrich and R. Torge, “Measurement of Thin Film Parameters with a Prism Coupler,” *Applied Optics*, vol. 12, pp. 2901–2908, December 1973.

[57] P. J. Chandler and F. L. Lama, “A New Approach to the Determination of Planar Waveguide Profiles by Means of a Non-stationary Mode Index Calculation,” *Journal of Modern Optics*, vol. 33, pp. 127 – 143, February 1986.

[58] I. Fatadin, D. Ives, and M. Wicks, “Accurate magnified near-field measurement of optical waveguides using a calibrated CCD camera,” *Journal of Lightwave Technology*, vol. 24, pp. 5067–5074, December 2006.

Acknowledgement

At the end of my doctoral studies I wish to thank Prof Paolo Bassi for the confidence granted me during this three years of training.

Other important thanks go to Prof Gian Giuseppe Bentini for the estimation shown to me.

I wish to thank also all the people without whom this work couldn't be possible in particular Dr. Marco Bianconi, Ing. Simone Sugliani, Dr. Pietro De Nicola and Dr. Marco Chiarini.

Moreover all the CNR-IMM technology department staff in particular Ing. Pera Maccagnani, Mr. Fabrizio Tamarri, Ing. Fulvio Mancarella, Mr. Giulio Pizzocchero, Dr Stefano Zampolli and Dr. Ivan Elmi.

The people of the DEIS department in particular Prof. Giovanni Tartarini, Dr Marco Gnan and Ing. Davide Visani.

And last but not the least Dr. Gaetano Bellanca.